Low Mass Clumps in TMC-1: Scaling Laws in the Small Scale Regime

R. Peng, W. D. Langer, T. Velusamy, T. B. H. Kuiper, S. Levin
MS 169-506
Jet Propulsion Laboratory
California Institute of Technology
Pasadena, CA 91109

ABSTRACT

We present new observational data on the small scale structure of the Taurus Molecular Cloud 1 (TMC-1) in the regime of 0.02-0.04 pc and 0.04 -0.6 $M_\odot$. Our analysis is based on high resolution, high signal-to-noise, observations of an $8' \times 8'$ area centered on the "cyanopolyyne peak" in the SE part of the TMC-1 ridge. The observations were made in the CCS 22 GHz and 45 GHz transitions using NASA's Deep Space Network 70-m and 34-m telescopes at the Goldstone facility. The CCS emission in this region originates in three narrow components centered on LSR velocities of ~5.7, 5.9, and 6.1 km S–l. These components each represent a separate cylindrical feature elongated along the ridge. Among the three velocity components we identified a total of 45 clumps with a typical CCS column density of ~ few x1013 cm^{-2}, an H_2 density of ~ few x104 cm^{-3}, and a mass in the range of 0.04 to 0.6 $M_\odot$. The statistical properties of these small scale clumps are compared with those of the larger "NH_3 cores" in cold clouds and "CS cores" in the hotter Orion region. The CCS clumps in TMC-1 are found to conform to the Larson's scaling laws (relating observed linewidth to clump size) derived from the larger cores down to the small scale regime (0.02 pc and 0.04 $M_\odot$). These clumps represent a regime where microturbulence is small, amounting to ~10% of the thermal pressure inside a clump. Of the 45 clumps, only five appear to be gravitationally unstable to collapse. The 6.1 km S-l component contains all the gravitationally unstable clumps and is the most likely site for future star formation.

Subject headings: ISM: clouds - ISM: individual (Taurus Molecular Cloud) - ISM: molecules - stars: formation - radio lines: ISM

1. Introduction

The mechanisms by which interstellar clouds produce the star forming cores is not well understood owing in part to the lack of sufficient data to draw a complete time line of the formation of these cores. Two such schemes have been proposed: gravitational fragmentation of larger structures or coalescence of smaller fragments formed from turbulent cascade. Larson (1981) found from a wide variety of molecular clouds an empirical correlation between the observed line width, cloud size, and the gas density, which was latter known as Larson's Laws. Although the physical basis of Larson's scaling laws is not well understood, the self-similar structure of molecular clouds as described by the Larson's Laws has been argued by many authors as turbulent in nature (see e.g. Goodman et al. 1997 and references therein).

In the cores of cold dense clouds there are many examples of line widths measured with trace molecules, such as CS, NH_3, HC_3N, that are narrower than the thermal line width of molecular hydrogen at 10 K (Fuller & Myers 1992, 1993, and Langer et al. 1995). In these cases the velocity field is mainly thermal and has a small non-thermal component which is probably due to microturbulent (subsonic) motions. Thermal H_2 pressure provides the main support for the cores. This situation is in contrast to cores in warmer molecular clouds where non-thermal components (likely macro-turbulence) dominate the velocity field as well as core support. These observations of small scale thermal features in cold dense clouds raise some important questions regarding the origin of the cold cores.

TMC-1 has been a prime object for studying cold cores because of its proximity and small velocity dispersion. To study the small scale structure of a quiescent dark cloud, such as TMC- 1, one needs to have sufficient spatial resolution, as well as high enough spectral resolution to sample molecular lines of thermal width (typically $\sim$ 0.1 km S–l for CCS in cold, dark clouds). There have been a number of studies of the structure of TM C-1 in a variety of tracers (e.g. Hirahara et al 1992, Onishi et al. 1996). Recently Langer and co-workers extended these studies to small scale structures through single-dish and interferometric observations of CS and CCS (Langer et al. 1995) and from multi–transition analysis of CCS (Wolkovitch et al. 1997). Using a heavy molecular tracer (CCS) with narrow thermal line-widths ($\sim$0. 1 kms^{-1} at $\sim$10 K), Langer et al. (1995) have shown that little turbulence is seen in the small scale structures in TMC-1. Therefore the small scale clumps in TMC-1 can be used to study the behavior of the scaling laws down to smaller sizes and masses, in a regime of low turbulence, where the turbulent widths are $\sim$0. 1 km S-l.

Here we present an extension of the earlier work by Langer et al. (1995) and Wolkovitch et al. (1997), consisting of better sampled and more extensive maps of CCS centered on the "cyanopolyyne peak" in the southeast part of the TMC-1 ridge. CCS is reasonably

abundant and widely distributed in TMC-1 (Hirahara et al. 1992, Langer et al. 1995, Wolkovitch et al. 1997), making it an excellent tracer for moderate density ($n(H_2) \gtrsim 10^4$ cm^{-3}) molecular gas.

From these high signal-to-noise, high spectral and spatial resolution maps we are able to identify more small scale clumps than seen in earlier work. The properties of these clumps are determined from an excitation analysis. The large number of clumps, 45 in total, makes it possible to evaluate their statistical properties and to test the Larson's scaling law in a small scale, low-mass regime. Of the 45 clumps identified in the area, only five are gravitationally unstable to collapse while the remainder are evenly split between unbound and stable objects. All the unstable clumps are associated with one spatial-velocity feature near the cyanopolyyne peak. Our results show that Larson's scaling laws extend down to the low mass clumps in TMC-1.

2. Observations and Data Reduction

Observations of the CCS 22 GHz and 45 GHz transitions were made with the Deep Space Network (DSN) 70-m and 34-m telescopes at the NASA Goldstone Facility over the period from April 1994 to March 1997. The 70-m telescope observations used a K-Band HEMT receiver tuned to the rest frequency of the CCS $J_N = 2_1 \rightarrow 1_0$ transition (22344.033 MHz). The system temperature is $\sim$70 K and the FWHM antenna beam is 45". Observations of the CCS $J_N = 4_3 \rightarrow 3_2$ transition (45379.033 MHz) using the 34-m beam waveguide telescope equipped with a Q-Band HEMT receiver were made with a typical system temperature of $\sim$130 K and a comparable FWHM beamwidth of 50". Both the 22 GHz and 45 GHz observations utilize the same backend, consisting of a Wide Band Spectrum Analyzer (WBSA; Quirk et al. 1988) covering a bandwidth of 40 MHz with over two million channels. We used a subset of 5 MHz in the middle of the WBSA for both the 22 GHz and 45 GHz observations, producing spectra of 8192 channels with a spectral resolution of 0.008 km S–l and 0.004 km S-l, respectively. The spectra were further smoothed to a resolution of 0.024 km S-l.

Extensive mapping was made at the CCS 22 GHz transition over an area of 8' x8' centered on the cyanopolyyne peak of TMC-1 RA(1950) = $04^h38^m42^s.0$, DEC(1950) = $25°34'50''.0$, the Core D region of Hirahara et al. (1992), at a spacing of 25" (Nyquist sampled). Observations of the CCS 45 GHz transitions were made towards peaks of the clumps identified from the CCS 22 GHz maps (see section 3), Observations at both frequencies were conducted in a position switching mode with four on-positions between two adjacent off-positions. A 10-min on-source integration at 22 GHz yields a rms noise

level of $\sim$ 0.06 K at a resolution of 0.024 kms-^{1}, while a comparable rms noise level is achieved at 45 GHz with a 20-min on-source integration after smoothing the spectra to the same resolution.

Calibration of the antenna temperature for each observing session was made with a noise diode and an ambient load. Corrections for atmospheric emission and absorption, as well as antenna gain variations over elevation angles were made in a self-consistent fashion. A reference position (the cyanopolyyne peak) was observed once every hour during each track. Scaling factors were calculated by comparing these values to that obtained with the NRO 45-m telescope towards the same position (Suzuki et al. 1992, Hirahara et al. 1992). The spectra taken at other positions were then scaled accordingly. Standard spectral line operations, such as co-adding spectra taken at the same position and removal of linear baselines, were performed on all the spectra.

3. Results

All the CCS spectra show evidence of a complex line shape best explained by three velocity components (cf. Langer et al. 1995). We show in Figure 1 representative spectra of CCS at both 22 GHz and 45 GHz towards three different positions in the Core D region of TMC1. To extract the structure and gas properties of these features separately we fitted each spectrum with three gaussian profiles. The spectral decomposition is conducted as follow: one gaussian is fitted to each line wing of the observed profile, and is subsequently subtracted from the line profile; the remaining part is fitted with a third gaussian. An example of the spectral decomposition is shown in the middle panels of Figure 1, with dotted lines showing the gaussian fits and residuals plotted at the baseline level in solid lines. The velocities of the fitted gaussian components generally group around LSR velocities centered at 5.7, 5.9, and 6.1 km s^{-1}. The gaussian components have FWHM line widths in the range of 0.14 to 0.23 km s^{-1}, as compared to 0.09 km s^{-1} for the thermal broadening of the CCS lines at 8 K.

3.1. Spatial–Velocity Distribution of 22-GHz CCS Emission

The distribution of CCS emission separates into three features each delineating an elongated structure oriented along the SE-NW direction. Figure 2 shows the distribution of integrated intensity of the three components. Molecular gas traced by the CCS 22 GHz transition largely follows that seen in other carbon-chain molecular line emission in the

TMC-1 ridge. Allthree components indicate little extension to the SE beyond the map, but inthe NWthere is clearly CCS emission beyond the mapped region extending towards the NH_3peak in the northwest ridge. The 5.9 km s^{-1} component appears to trace a narrow strip along the "crest" of the TMC-1 ridge. Overall, maps of the three components have an elongated appearance along the ridge, which may represent a cylindrical structure for each component. Each one of the cylindrical components is very clumpy as can be seen in the individual maps in Figure 2.

We identified 45 clumps in the maps for the three velocity components. As marked in Figure 2, most of these are clearly evident by visual inspection. The high signal-to-noise ratio (> 20) of the spectra allows us to decompose even the few cases of significant spatial overlapping (e.g. b14 & 15; r9, 10 & 11). Following the methodology of CLUMPFIND (Williams et al. 1994), we trace out gaussian profiles for peaks above the 5σ level. Some areas clearly show significant overlapping of these gaussian clumps. In such cases, we carefully inspect the contour topology at relatively lower levels (i.e. at and around the half-maximum level) to examine the number and size of gaussian components that will fit into the contour envelope. Each clump is characterized by its peak position and the major and minor axes of the FWHM area. The clumps are marked in Figure 2 and listed in Table 1. Clumps are grouped in Table 1 by their velocity, with the designation: b (blue), m (middle), and r (red) refer to the 5.7, 5.9, and 6.1 km s^{-1} velocity features, respectively. The clumps are numbered along the ridge from NW to SE. The position of each clump is shown in the second and third column of Table 1 as offsets in RA and Dec. to the reference position, $RA(1950) = 04^h38^m42^s.0, Dec(1950) = 25°34'50''.0$ (CCS peak). The table also lists the major and minor axial size, the peak brightness temperature T_R, center velocity v_{LSR}, and the FWHM line width w of the CCS 22 GHz spectrum determined at the peak of each clump.

3.2. H_2 Density and CCS Column Density

From the peak brightness temperature T_R at 22 and 45 GHz we derive the gas density and CCS fractional abundance in the individual clumps using an excitational analysis. The CCS model calculations of Wolkovitch et al. (1997) were used with a fixed kinetic temperature of 8 K, which appears representative for the SE part of the TM C-1 ridge. The values of $X/(dv/dr)$, the ratio of CCS fractional abundance (X), and the velocity gradient across the cloud (dv/dr) were obtained from the LVG calculations. We find $X/(dv/dr)$ to be tightly clustered for clumps within each cylindrical component (see Table 2), indicating a roughly constant CCS fractional abundance for each component. This result allows us

to simplify derivations of CCS column density and mass by adopting an average value of $X/(dv/dr)$ for all clumps, and deriving the H_2 density $(n(H_2))$ for each clump using only the T_R at 22 GHz, $N_{CCS} \sim n_{H_2}(X/(dv/dr))\Delta v$ cm^{-2}. The results are listed in Table 1.

3.3. Clump Mass

The mass of each clump is

$$M \sim 1.15 \times 10^{-26} N_{H_2} b_{maj} b_{min} M_{\odot} \quad (1)$$

where b_{maj} and b_{min} are the major and minor axes of the FWHM size of the clump in arcsecond; NH, is the H_2 column density toward the clump, Equation (4) includes the contribution from helium assuming a fractional abundance of 0.1 relative to hydrogen nuclei. N_{H_2} is derived from

$$N_{H_2} \sim \frac{N_{CCS}}{X}. \quad (2)$$

We used the average fractional abundance, (X), for the three velocity features as given in Table 2. The clump masses are listed in Table 1.

4. Discussion

TMC-1 has been well studied because of its unique morphology and chemical inhomogeneities. Many interesting models have been proposed to explain these aspects of the cloud, for example, cloud collision (Little et al. 1978) and sequential star formation along the ridge (Hanawa, Yamamoto, & Hirahara 1994). In this paper we will not attempt to interpret the chemical and physical properties of the TMC-1 ridge, but restrict our discussion to the new observational data on the small scale clumps in the SE part of the ridge as traced by CCS.

4.1. Statistical Properties of the CCS Clumps

What are these low mass clumps in TMC-1 as traced by the CCS emissions and what is their significance to star formation? To answer these questions, it is important to compare the physical characteristics of these clumps with those of the other star forming cores such as the cold cloud "NH_3 cores" of Benson & Myers (1989) and the hotter CS cores in Orion-A (Tatematsu et al. 1993). In Figure 3 we plot in logarithmic scale the observed FWHM line widths versus mass and radius of all clumps and cores.

In the left panel of **Figure 3** we show theplotof line width versus clump mass. The thick dashed line in the figure represents a power law fit of the form: $\Delta V_{obs} \propto M^{\alpha}$ where $_0$! = 0.23 is the fit for the Orion-A CS cores by Tatematsu et al. (1992). The Orion-A CS cores aregenerally invirial equilibrium, andnon-thermal pressure provides the main support in a core, judging from the observed line width in comparison with the estimated thermal broadening of molecular hydrogen. Clearly, dense cores in cold dark clouds follow a different power law. For the NH_3 cores and small scale CCS clumps, we find

$$\Delta V_{obs} \sim 0.22 M^{0.14} \quad (3)$$

where the linear correlation coefficient is 0.79. The fit is shown as a thick dotted line. The different linewidth versus mass relation for the dark cloud cores and small scale clumps may reflect the fact that non-thermal pressure plays a substantially smaller role in supporting the cores compared to their counterparts in Giant Molecular Clouds (GMC's). In addition, there is an increasing proportion of small scale clumps departing from virial equilibrium as one moves into the small scale regime in dark molecular clouds (see Section 4.2).

In the right panel of Figure 3 we show the plot of observed line width versus size of cores and clumps. The thick dashed line in the right panel shows Larson's Laws (Larson 1981) as applied to dense cores in Orion-A, $\Delta V_{obs} \sim 2.5 R^{0.4}$, from Tatematsu et al. (1992). We also fit the NH_3 cores and CCS clumps in dark clouds with a power law,

$$\Delta V_{obs} \sim 0.69 R^{0.39} \quad (4)$$

where the linear correlation coefficient is 0.87. The fit is shown as a thick dotted line. It agrees with those derived for dark cloud cores by Fuller & Myers (1992) with a power index of 0.4 and 0.44 for cores with and without stars, respectively. The plot clearly shows that Larson's Law still hold for structures in dark clouds down to a scale of -0.02 pc.

The result that the same scaling law applies to dense cores in both GMC's and cold dark clouds implies that these two kinds of clouds share the same mechanism of fragmentation, either turbulent cascade or gravitational fragmentation, or both. It is also evident that GMC's and dark clouds have different velocity dispersion coefficients in the Larson's Laws (2.5 and 0.69, respectively). This variation is an indication of the different energy content in the cascading structures in GMC's and dark clouds, with GMC's being more energetic.

With a sizable number of clumps identified around the cyanopolyyne peak in the SE region of TMC-1, we can also study the mass distribution of clumps in the low-mass regime. In Figure 4 we plot the number of clumps at each mass interval and fit it with a power law,

$$N \sim 1.6 M^{-0.56} \quad (5)$$

which is shown as a solid line in the figure. The corresponding mass spectrum index $dN/dM = -1.56$ is in good agreement with those obtained for cores of large mass (M $\gtrsim$ 20 $M_\odot$) in various GMC's ($\sim$ – 1.6, see Blitz 1991 and references therein). This compares to a mass spectrum index of – 1.2 for dark cloud cores of Myers, Linke, & Benson (1983) and -0.9 for $C^{18}O$ cores in Taurus molecular cloud (Onishi et al. 1996). Onishi et al. argued for a flatter mass spectrum in the low mass range, which does not appear to bear out in our results for the CCS clumps with masses typically smaller than 0.5 $M_\odot$.

4.2. Dynamical Status of the CCS Clumps

To assess the dynamical status of each clump with regard to gravitational collapse, we calculate the virial mass for each clump in two limiting cases (MacLaren et al. 1988):

$$M_{vir} \sim 7\ R(\Delta v_{av})^2\ M_\odot \qquad (6)$$

where 7 $\sim$ 210 for constant density distribution, and 7 $\sim$ 126 for r^{-2} density distribution in the clump. R is the average radius of the clump listed in Table 1, and is calculated by

$$R \sim 4.07X\ 10^{-4} \sqrt{b_{maj} b_{min}}\ pc, \qquad (7)$$

where b_{maj} and b_{min} are the major axes of the clump in arcsec. A distance of 140 pc is used for TMC-1 in the above calculation. Δv_{avg} is the line width of the average (mainly H_2) gas of the clump,

$$\Delta v_{avg} = 2.35 \sqrt{\sigma^2_{turb} + \sigma^2_{therm}\ (H_2)} \qquad (8)$$

where

$$\sigma_{therm} = 0.091 \sqrt{\frac{T_K}{m_{mau}}}\ km\ S\text{-}l \qquad (9)$$

and m_{mau} = 2.3 for average gas. The velocity dispersion resulting from turbulent motions in the clump, σ_{turb}, is obtained using the measured line width and the thermal dispersion of CCS with m_{mau} = 56:

$$\Delta v_{obs} = 2.35 \sqrt{\sigma^2_{turb} + \sigma^2_{therm}\ (CCS)}\,. \qquad (10)$$

Two estimates of M_{vir} for each clump are listed in Table 1, depending on the assumed density profile.

Clearly, a clump is more prone to gravitational collapse if it has a centrally condensed structure rather than a uniform density profile, as the viral mass in the first case is substantially smaller. When M > M_{vir}, a clump is gravitationally unstable, and is likely to collapse. If 0.5 M_{vir} < M < M_{vir}, it is stable. If M < 0.5 M_{vir}, a clump is gravitationally

unbound. We use the notation "BC", "S", and "UB" in Table 1 to represent the three cases of being bound and capable of collapse, stable, and unbound. Of the 45 clumps, 19 appear to be gravitationally unbound; 21 are stable and only five are likely to collapse under their own gravity. If the clump mass is compared against the virial mass of a uniform clump, then all the clumps in the 5.7 km s^{-1} component and most of those in the 5.9 km s^{-1} component would become gravitationally unbound, and all the clumps in the 6.1 km s^{-1} component would be stable.

It is interesting to note that the 6.1 km s^{-1} component contains all the clumps that are likely to undergo gravitational collapse. This suggests that it is in a relatively more advanced evolutionary stage than the other velocity components. It also corroborates the fact that high resolution VLA observations of a portion of the region (Langer et al. 1995 and Velusamy 1997) see only condensations in the 6.1 km s^{-1} component. Clearly, the 6.1 km s^{-1} component is the most likely center of future star forming activity in the region. Note that all five candidates for core collapse have masses in the range of 0.5-0.6 $M_{\odot}$, indicating a future population of low mass stars.

It is also interesting that at least 19 (and perhaps up to 30) out of 45 clumps in the region are gravitationally unbound. Such a finding comes as no surprise because this region in the TMC-1 ridge indeed lacks star forming activity. Previous studies of cores in the TMC-1 ridge with coarser spectral and spatial resolutions (e.g. Hirahara et al. 1992 and Onishi et al. 1996) generally find fewer but larger cores all of which appear to be gravitationally bound. One of these cores, Core D, (Hirahara et al. 1992) is now resolved into 45 small clumps. Among them a substantial portion are gravitationally unbound. This result may indicate a break down of the self-similar structure of molecular clouds (Falgarone, Phillips, & Walker 1991) as one probes the physical regime where thermal pressure inside a clump is dominant over that of non-thermal pressure (by a factor of ~ 10 for the CCS clumps).

The unbound clumps, if not confined by an external pressure, would disperse at the sound speed of ~ 0.3 km s^{-1} over a time scale of $\sim 2 \times 10^5$ yr, which compares to a molecular cloud's lifetime of $\gtrsim 10^6$ yr. As gravitationally unbound clumps appear in such a large proportion, they cannot all be transient in nature. We suggest that thermal and turbulent pressures of the interclump gas may contribute to keep these clumps pressure-bound.

To estimate the external pressure required to confine an unbound clump, we calculated the virial parameter (Bertoldi & McKee 1992) for each clump:

$$\alpha = \frac{5\sigma_{av}^2 R}{GM}. \qquad (11)$$

This parameter measures the relative importance of internal kinetic energy and the

gravitational potential, and is within a factor of 1 to 1.3 of the ratio of internal kinetic energy and gravitational potential of the clump. Assume the clumps are in a quasi-virial equilibrium whereby the internal kinetic energy is in balance with the gravitational potential and the surface energy exerted by ambient gas pressure, We can estimate the temperature of the interclump gas T_{ic} required to confine the clumps if the external pressure is only of thermal origin:

$$T_{ic} = (1 - \frac{a}{a})\frac{n_{cl}}{n_{ic}} T_{cl} \quad K \tag{12}$$

where the factor a ranges between 1 and 1,3, n_{ic} is the gas density of the interclump gas, n_{cl} and T_{cl} are the gas density and kinetic temperature of the clump, respectively.

For the unbound clumps listed in Table 1, the virial parameter ranges between 5.6 to 17.9 with a median value of $\sim$9.5. The interclump gas probably has a density of $\sim 2\times 10^3$ c m^{-3} as seen in $C^{18}O$ emission of the region (Langer et al. 1995). With a clump temperature of 8 K and a clump density of $\sim 10^4$ cm^{-3}, the interclump gas would need to have a temperature of $\sim$ 40 K to confine the clumps with thermal pressure. Such a temperature appears to be too high by at least a factor of two than the interclump gas temperature as estimated from the $C^{18}O$ observation. On the other hand, microturbulence in the interclump gas may provide enough pressure to confine the clumps. The $C^{18}O$ observations of the region (Langer et al. 1995) shows a typical line width of 0.45 km s^{-1}, within which the thermal broadening accounts for only $\sim 1/4$ of the line width. The remaining part would be due to microturbulence in the interclump gas, which would have a turbulent pressure equivalent to the thermal pressure at a gas temperature of 75 K to 100 K, enough to confine the unbound clumps.

4.3. Relative Motion Among CCS Clumps

The high spectral resolution and the high signal-to-noise ratio obtained for the CCS spectra enable us to determine the clump velocities to a high degree of precision and hence to study the relative movement among the clumps within each of the three cylindrical features in the TMC-1 ridge. As seen in Tables 1 and 2, the velocities of the clumps in each feature have a small dispersion about the mean with a standard deviation of 0.03 km s^{-1}. This amounts to a random motion among the clumps of the order 0.05 km s^{-1}, assuming an isotropic random velocity distribution. At such a small relative velocity, it would take $\gtrsim 2.4 \times 10^6$ yr for a clump to migrate across the ridge of $\sim$ 3' ($\sim$0. 12 pc) in width, and four to five times longer to travel from one end to the other along the ridge.

It is interesting to compare the above crossing time with the collision time over which a

clump is likely to encounter another clump in the same cylindrical component. To calculate the collision time, we estimate the average separation between clumps as

$$\Delta l \sim 2(\frac{1}{\sqrt[3]{\gamma}} - 1)r, \quad (13)$$

where r is the clump radius, and γ is the clump filling factor in each component. γ is estimated by:

$$\gamma \sim \frac{n_{clump} V_{clump}}{V_{comp}}, \quad (14)$$

where n_{clump} is the number of clumps in the cylindrical component, V_{clump} is the average volume of each clump, and V_{comp} is the volume of the component. Assuming a cylindrical geometry for the component and spherical geometry for the clumps, the clump filling factor is estimated to be 0.11, 0.19, and 0.07 for the 5.7, 5.9 and 6.1 km s^{-1} features, respectively. The average separation Al is then $\sim$0.07, 0.04, and 0.08 pc, respectively, and the corresponding collision time is 1.3x106, 8.9x105, and 1.7x106 yr.

Comparing different time scales (τ(dispersion) $\sim$ 2x105 yr, τ(collision) $\sim$ 1x106 yr, and τ(crossing) > 2x106 yr), it would seem that a CCS clump is more likely to be subject to merging or fragmenting due to collisions with other clumps rather than traveling intact along the ridge. On the other hand, clumps do move around appreciably within each cylindrical component over their lifetime, providing sufficient mixing for a homogeneous temperature and chemical abundance distribution in each cylindrical component.

4.4. Comparison of the Three Velocity Features

We list in Table 2 the average values of $v_{LSR}, w, dv/dr, n_{H_2}$, and N_{cc}s for the clumps in each velocity component. The associated errors are standard deviations. Also listed are average values of $\log(X/(dv/dr))$ and X. The error associated with $\log(X/(dv/dr))$ reflects the scatter of the clump distribution on a $\log(n_{H_2})$ versus $\log(X/(dv/dr))$ plot, the error for X is the compound error of $\log(X/(dv/dr))$ and (dv/dr). The total mass of molecular gas traced by CCS in each cylindrical component is also given in the table. We summarize in Table 2 the total number of bound and unbound clumps in each velocity feature.

As seen in Figure 2, the components have a different overall structure in the CCS emission. The 5.7 km S-l component is the most extended among the three. It also has on average a broader CCS line width and a markedly higher CCS fractional abundance than the other two (see Table 2). A higher CCS abundance has been related to young dense material in dynamical models (Kuiper et al. 1996; Bergin & langer 1997). In addition,

the predominance of the unbound clumps in the 5.7 and 5.9 km s^{-1} features is consistent with the interpretation that they trace gas at a relatively younger evolutionary phase than the 6.1 km s^{-1} feature. Overall, the 5.7 km s^{-1} component seems to be a loosely structured cloud with relatively new gas of moderate density. The 6.1 kms-1 component, in comparison, appears more evolved with a tightly confined structure.

5. Conclusion

We have mapped an $8' \times 8'$ area around the cyanopolyyne peak in the nearby dark cloud TMC-1 in the CCS 22 GHz transition with Nyquist sampling and a 0.008 km s^{-1} velocity resolution. We combined this map with observations of the CCS 45 GHz transition to analyze its small scale structure. The region contains three major cylindrical features at LSR velocities of 5.7, 5.9 and 6.1 $km\,s^{-1}$. The 5.7 km s^{-1} cloud and the 6.1 km S-l components occupy similar areas in the sky along the TMC-1 ridge, while the 5.9 km s^{-1} component is more spatially confined.

Using a multi-gaussian spectral decomposition and spatial-spatial maps we identified 45 clumps in the three velocity components. Most of the clump masses range from 0.1 to 0.5 MO, while a few are much smaller, $\sim$ 0.05 MO. The CCS line width of the clumps ranges from 0.14 to 0.23 km s^{-1}, with microturbulence in the clump contributing $\sim$ 1/4 of the H_2 line broadening.

The CCS clumps in TMC-1 indicate that Larson's scaling laws still hold in the small scale regime down to 0.02 pc and 0.04 MO.

Out of the 45 clumps, only five are likely to be gravitationally unstable to collapse. The rest are stable or unbound and the predominance of these clumps is consistent with the low star forming activity in this region of the TMC-1 cloud.

R. P. is a National Research Council Research Associate at the Jet Propulsion Laboratory, California Institute of Technology. This research was conducted at the Jet Propulsion Laboratory, California Institute of Technology under support from the National Aeronautics and Space Administration. We would also like to thank the DSN operations staff for their assistance with the observations.

TABLE 1

CCS CLUMPS IN TMC-1 CORE D REGION

Clump[b]	Offset[b] arcsec	Size[c] arcsec	T_R K	V_{peak} km/s	w km/s	n_{H_2}[d] cm^{-3}	N_{CCS}[d] cm^{-2}	M[d] $M_\odot$	M_{vir}[e] MO	Note[f]
b1	-140,235	86x **76**	**2.0**	5.768	0.211	7.6(3)	1.6(13)	**0.12**	0.640.38	U B
b2	-136,181	83x61	2.1	5.738	**0.194**	8.3(3)	1.6(13)	0.09	0.560.34	**UB**
b3	-106,161	**89×** 67	2.4	5.750	0.184	9.8(3)	1.8(13)	0.13	0.61 0.36	UB
b4	-141,124	91x69	3.4	5.701	0.186	1.8(4)	3.3(13)	0.24	0.620.37	S
b5	-104,100	**89×** 80	3.1	5.714	0.216	1.5(4)	3.2(13)	0.27	0.660.40	S
b6	-75, 84	70x61	**2.9**	**5.696**	0.211	1.3(4)	2.7(13)	0.14	0.520.31	U B
b7	–50, 55	86X61	3.0	5.693	0.205	1.5(4)	3.0(13)	0.19	0.570.34	S
b8	–107, 41	84x 70	3.3	5.681	0.232	1.7(4)	3.8(13)	0.27	0.61 0.36	S
b9	-80, 24	89x 73	3.4	5.676	0.217	1.8(4)	3.8(13)	0.30	0.630.38	S
b10	-49, 16	86x 70	3.6	5.705	0.194	2.0(4)	3.8(13)	0.27	0.610.37	S
b11	3,-1o	80x68	3.5	5.713	0.162	1.8(4)	2.8(13)	0.18	0.580.35	S
b12	9,-52	83x64	3.7	5.705	0.160	2.1(4)	3.3(13)	0.21	0.570.34	S
b13	-53,-78	67x56	2.0	5.654	0.216	7.6(3)	1.6(13)	0.07	0.480.29	**UB**
b14	41,-85	89 x64	3.3	5.711	0.156	1.7(4)	2.6(13)	0.18	0.590.36	S
b15	48,-115	89 x63	3.2	5.685	0.152	1.7(4)	2.5(13)	0.17	0.590.35	**UB**
b16	81,-149	86x 79	2.9	5.670	0.163	1.4(4)	2.2(13)	0.18	0.650.39	**UB**
b17	124,-185	92x61	2.5	5.656	0.203	1.1(4)	2.2(13)	0.15	0.590.35	**UB**
m1	–212, 232	67x56	2.8	5.869	0.162	3.5(4)	1.7(13)	0.25	0.480.29	S
m2	-176,164	83 x63	1.8	5.929	0.169	1.8(4)	9.4(12)	0.18	0.570.34	S
m3	-150,104	69x52	1.3	5.908	0.169	1.1(4)	5.7(12)	0.08	0.470.28	**UB**
m4	-80, **84**	68x 59	1.0	5.864	0.180	8.9(3)	4.9(12)	0.07	0.500.30	**UB**
m5	-120, 74	67x52	1.2	5.855	0.176	1.1(4)	6.0(12)	0.08	0.470.28	**UB**
m6	–117, 39	61x49	0.9	5.832	0.161	7.2(3)	3.6(12)	0.04	0.430.26	**UB**
m?	-76, 26	70x61	1.2	5.856	0.171	1.1(4)	5.8(12)	0.09	0.520.31	**UB**
m8	-40, –3	89x57	**1.4**	5.879	0.166	1.3(4)	6.7(12)	0.13	0.560.34	**UB**
m9	**9,** -8	73x61	1.9	5.880	0.156	2.0(4)	9.6(12)	0.16	0.530.32	S
m10	12,-53	75 x67	2.5	5.888	0.145	3.1(4)	1.4(13)	0.26	0.560.34	S
m11	35,-84	70X53	1.9	5.907	0.155	2.0(4)	9.6(12)	0.14	0.480.29	**UB**
m12	0,-109	76X 50	1.5	5.886	0.156	1.4(4)	6.7(12)	0.10	0.490.29	**UB**
m13	46,-140	80X 53	1.2	5.936	0.163	1.1(4)	5.5(12)	0.09	0.510.31	**UB**
m14	99,-180	89 x69	1.3	5.929	0.139	1.2(4)	5.2(12)	0.12	0.620.37	**UB**
m15	128,-196	73 x56	0.9	5.903	0.153	8.1(3)	3.8(12)	0.06	0.500.30	**UB**
r1	-112,235	92X 64	1.8	6.105	0.177	3.0(4)	1.0(13)	0.40	0.600.36	**BC**
r2	-80,181	97x68	1.6	6.090	0.172	2.4(4)	8.0(12)	0.35	0.640.38	S
r3	-121,142	82X 76	1.7	6.004	0.161	2.6(4)	8.1(12)	0.34	0.620.37	S
r4	-76,121	86X61	2,0	6.067	0.147	3.4(4)	**9.7(12)**	0.34	0.570.34	**BC**
r5	-33, **95**	78X 63	1.9	6.074	**0.149**	3.3(4)	9.6(12)	0.31	0.550.33	s
r6	-109, 61	58X 52	1.4	6,003	0.178	2.1(4)	7.3(12)	0.15	0.440.26	S
r7	-10, 52	83x 76	2.4	6.084	0.169	4.5(4)	1.5(13)	0.62	0.630.38	B C
r8	-46, 21	86X 63	1.8	6.072	**0.165**	2.9(4)	9.3(12)	0.33	0.580.35	S
r9	6, -7	73x55	2.1	6.054	0.151	3.7(4)	1.1(13)	**0.29**	0.500.30	s
r10	28,-35	86 x64	**2.0**	**6.040**	**0.160**	3.5(4)	1.1(13)	0.40	0.580.35	**BC**
r11	3.-36	**70×67**	2.3	**6.044**	**0.149**	4.4(4)	1.3(13)	0.40	0.540.33	**BC**
r12	70.-93	75x56	**1.9**	**6.010**	0.142	3.3(4)	9.1(12)	0.26	**0.51 0.31**	S
r13	27.-106	76x52	**1.6**	**6.008**	(-).159	2.5(4)	**7.7(12)**	0.20	0.500.30	S

[a] **Letters** b (blue), m (middle), **and** r **(red)** refer to the 5.7, 5.9, and 6.1 **km s^{-1} components**, respectively.
[b] **Peak offsets** in **arcsecond** relative to **RA(1950) 04^{h}38^{m}42^s.0, Dec(1950) 25°34′50″.0**
[c] Major and **minor axes (arcs econd) of** the FWHM **clump area**
[d] **Numbers** in parentheses **are exponents to** Hz density **and** CCS **column density**
[e] **Virial masses for** density **distribution of** the form: $\rho \sim r^a$, **where** $a=0, -2$ **respectively.**
[f] **UB: unbound; S: stable and bound; BC: bound and unstable, likely to collapse.**

TABLE 2

AVERAGE PROPERTIES OF THE THREE CCS COMPONENTS IN TMC-1 CORE D REGION

Layer	$\langle V_{peak} \rangle$[a] km/s	$\langle w \rangle$[a] km/s	$\langle \mathcal{X} \rangle$[b]	$\langle dv/dr \rangle$[c] km/s/pc	(X)[d] x 10^{-9}	$\langle n_{H_2} \rangle$ $\times 10^4$	$\langle N_{CCS} \rangle$ $\times 10^{12}$	M $M_\odot$	B/U[e]
5.7	km/s 5.70±0.03	0.19±0.02	−8.5±0.2	3.1±0.5	9.8±4.8	1.4±0.5	26.9±7.6	3.16	9/8
5.9	km/s 5.89±0.03	0.16±0.01	−9.0±0.2	3.1±0.4	3.1±1.5	1.5±0.8	7.6±3.7	1.85	4/11
6.1	km/s 6.05±0.03	0.16±0.01	−9.2±0.1	2.8±0.4	1.8±0.5	3.2±0.7	9.9±2.0	4.39	13/0

[a] Average peak velocity and line width of the CCS 22 GHz transition in each component

[b] Average and scatter of $\mathcal{X}(=\log(X/(dv/dr))$ found from fitting the clumps to LVG calculations

[c] Average velocity gradient for each component

[d] CCS fractional abundance for each component with compound errors of $\mathcal{X}$ and (dv/dr)

[e] The number of gravitationally bound and unbound clumps in each component

REFERENCES

Bergin, E. A., &Langer, W. D. 1997, ApJ, in press

Benson, P. J. & Myers, P. C. 1989, ApJS, 71, 89.

Bertoldi, F. & McKee, C. F. 1992, ApJ, 395, 140.

Blitz, L., 1991, in The Physics of Star Formation and Early Stellar Evolution, eds. C. J. Lada & N. D. Kylafis (Dordrech: Kluwer)

Falgarone, E., Phillips, T. & Walker, C. K. 1991, ApJ, 378, 186.

Fuller, G.& Myers, P.C. 1992, ApJ,384,523.

Fuller, G. & Myers, P. C. 1993, ApJ, 418, 272.

Goodman, A. A., Barranco, J. A., Wilner, D. J. & Hyers, M, H. 1997, ApJ, submitted

Hanawa, T., Yamamoto, S. & Hirahara, Y. 1994, ApJ, 420, 318.

Hirahara, Y., Suzuki, H., Yamamoto, S., Kawaguchi, K. & Kaifu, N. 1992, ApJ, 394, 539.

Kuiper, T. B. H., Langer, W. D., Velusamy, T, 1996, ApJ, 468, 761.

Langer, W. D., Velusamy, T., Kuiper, T. B. H., Levin, S., Olsen E., & Migenes, V. 1995, ApJ, 453, 293.

Little, L. T., Riley, P. W., Macdonald, G. H., & Matheson, D. N. 1978, MNRAS, 183, 805.

MacLaren, I., Richardson, K. M. & Wolfendale, A. W. 1988, ApJ, 333, 821.

Myers, P. C., Linke, R. A. & Benson, P. J. 1983, ApJ, 264, 517.

Onishi, T., Mizuno, A., Kamura, A., Ogawa, H. & Fukui, Y. 1996, ApJ, 465, 815.

Quirk, M. P., Wilk, M. F., Garyantes, M. F. & Grimm, M. J. 1988, IEEE Trans. on Acoustics, Speech & Signal Processing, 36, 1854.

Suzuki, H., Yamamoto, S., Ohishi, M., Kaifu, N., Ishikawa, S., Hirahara, Y. & Takano, S. 1992, ApJ, 392, 551.

Tatematsu, K., Umemoto, T., Kameya, O., Hirano, N., Hasegawa, T., Hayashi, M., Iwata, T., Kaifu, N., Mikami, H., Murata, Y., Nakano, M., Nakano, T., Ohashi, N., Sunada, K., Takaba, H. & Yamamoto, S., 1993, ApJ, 404, 643.

Velusamy, T. 1997, private communication.

Williams, J. P., de Geus, E., Blitz, L. 1994, ApJ, 428, 693

Wolkovitch, D., Langer, W. D., Goldsmith, P. F. & Heyer, M. 1997, ApJ, 477, 241.

This preprint was prepared with the AAS LaTeX macros v4.0.

Fig. 1.— Representative spectra of CCS at 22 GHz (top row) and 45 GHz (bottom row) towards three offset positions in the SE region of TM C- 1. Numbers in parentheses in the upper right corner of the top panels refer to the positional offset of the column in arcmin to the reference position at $RA(1950) = 04^h38^m42^s.0, Dec(1950) = 25\ °34'50''.0$. The spectra are sampled at a velocity resolution of 0.004 and 0.008 kms- ^{1} at 45 GHz and 22 GHz respectively, and are smoothed to 0.024 kms- ^{1}. The spectra show underlying narrow-line structures, representing at least three gas components along the line of sight. Spectral decomposition (see text) is demonstrated using the (O, O) spectra shown in the middle panels. The gaussian fits are shown in dotted lines, and residuals in solid lines at the baseline level.

Fig. 2.— Distributions of integrated CCS line intensity of the three velocity components in the Core D region around the cyanopolyyne peak in TMC-1. The central velocity of each component is shown in the topleft corner of each panel; the filled circle in the lower-right corner of the bottom panel shows the FWHM beam of the telescope. Contours represent fractional levels in the range of 15% to 99% of the peak of each map (0.87, 0.39, and 0.42 K km s^{-1} for the 5.7, 5.9 and 6.1 km s^{-1} components, respectively) with an increment of 5%. The gray scale reflects the same intensity range. Labels mark the clumps identified in each map.

Fig. 3.— CCS clumps in TMC-1 Core D region (as filled triangles, squares and circles) in the logarithmic plots observed line width versus clump mass (left panel) and clump radius (right panel). A sample of NH_3 cores in dark clouds (Benson & Myers 1989) and the CS cores in Orion A molecular cloud (Tatematsu et al. 1992) are also plotted for comparison as open diamonds and filled stars, respectively. The two horizontal dashed lines mark the sound speed (V_c) at 8 K and the thermal broadening of CCS molecule $(\Delta V_t(\mathrm{CCS}))$ at 8 K. The thick dashed line in the left panel shows a power law fit of $\Delta V_{obs} \sim 0.43 M^{0.23}$ for the Orion-A CS cores; the thick dotted line shows the fit for dark cloud NH_3 cores and TMC-1 CCS clumps $(\Delta V_{obs} \sim 0.22 M^{0.14})$. Similarly, the thick dashed line in the right panel represent Larson's scaling laws applied to the Orion-A CS cores (A $V_{obs} \sim 2.5 R^{0.4}$) and the thick dotted line shows the fit to the dark cloud cores and CCS clumps $(\Delta V_{obs} \sim 0.69 R^{0.39})$.

Fig. 4.— Mass distribution function of CCS clumps in TMC-1 Core D region shown as a histogram. The solid line represents the least-square fit of the mass distribution function.

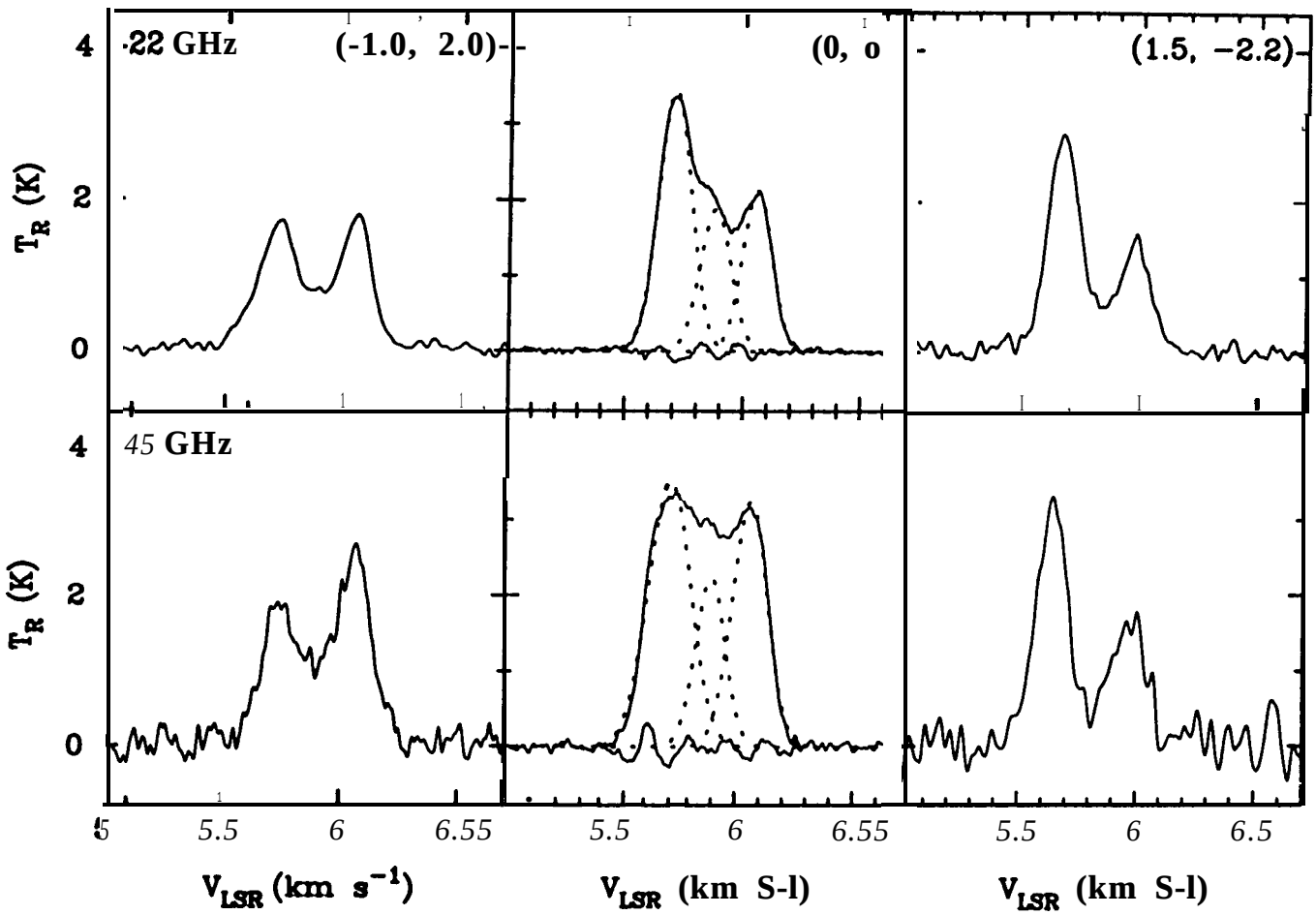
22 GHz
(-1.0, 2.0)
(0, o
(1.5, −2.2)
45 GHz
T_R (K)
4
2
0
5.5
6
6.55
6.5
V_{LSR} (km s^{-1})
V_{LSR} (km S-l)

FIGURE 1

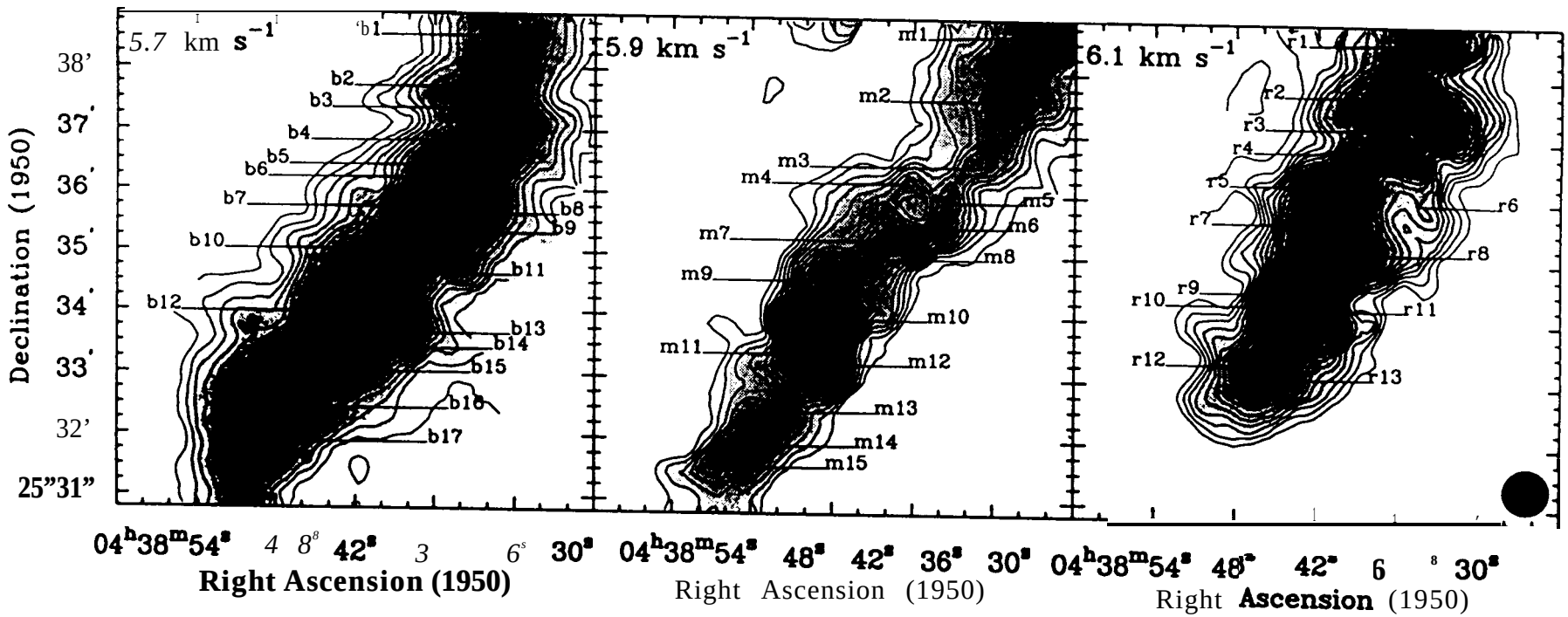
5.7 km s^{-1}
5.9 km s^{-1}
6.1 km s^{-1}
b1
b2
b3
b4
b5
b6
b7
b8
b9
b10
b11
b12
b13
b14
b15
b16
b17
m1
m2
m3
m4
m5
m6
m7
m8
m9
m10
m11
m12
m13
m14
m15
r1
r2
r3
r4
r5
r6
r7
r8
r9
r10
r11
r12
r13
Declination (1950)
38'
37'
36'
35'
34'
33'
32'
25"31"
04^{h}38^{m}54^s 42^s 30^s
Right Ascension (1950)
Right Ascension (1950)
Right Ascension (1950)

FIGURE 2

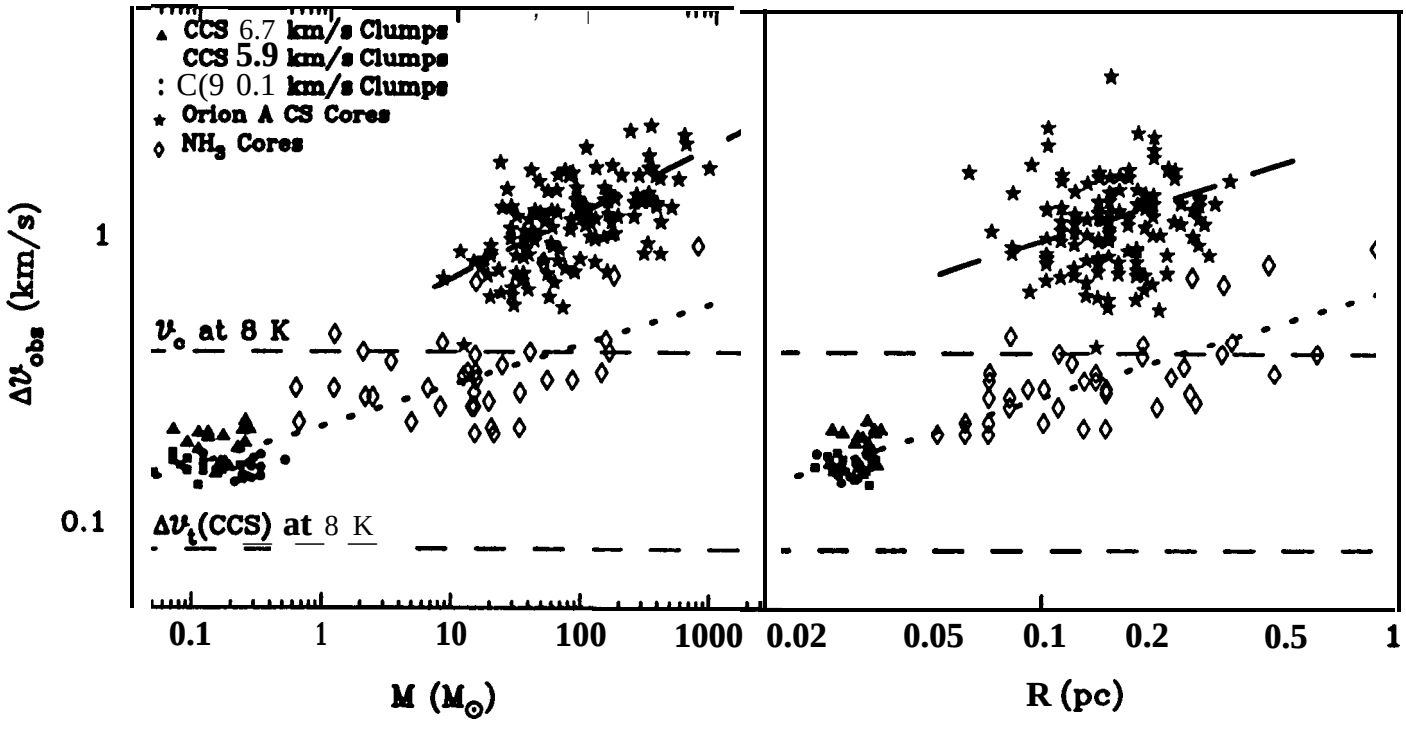
CCS 6.7 km/s Clumps
CCS 5.9 km/s Clumps
: C(9 0.1 km/s Clumps
Orion A CS Cores
NH3 Cores
v_o at 8 K
Δv_t(CCS) at 8 K
Δv_{obs} (km/s)
1
0.1
0.1
1
10
100
1000
M ($M_\odot$)
0.02
0.05
0.1
0.2
0.5
1
R (pc)

FIGURE

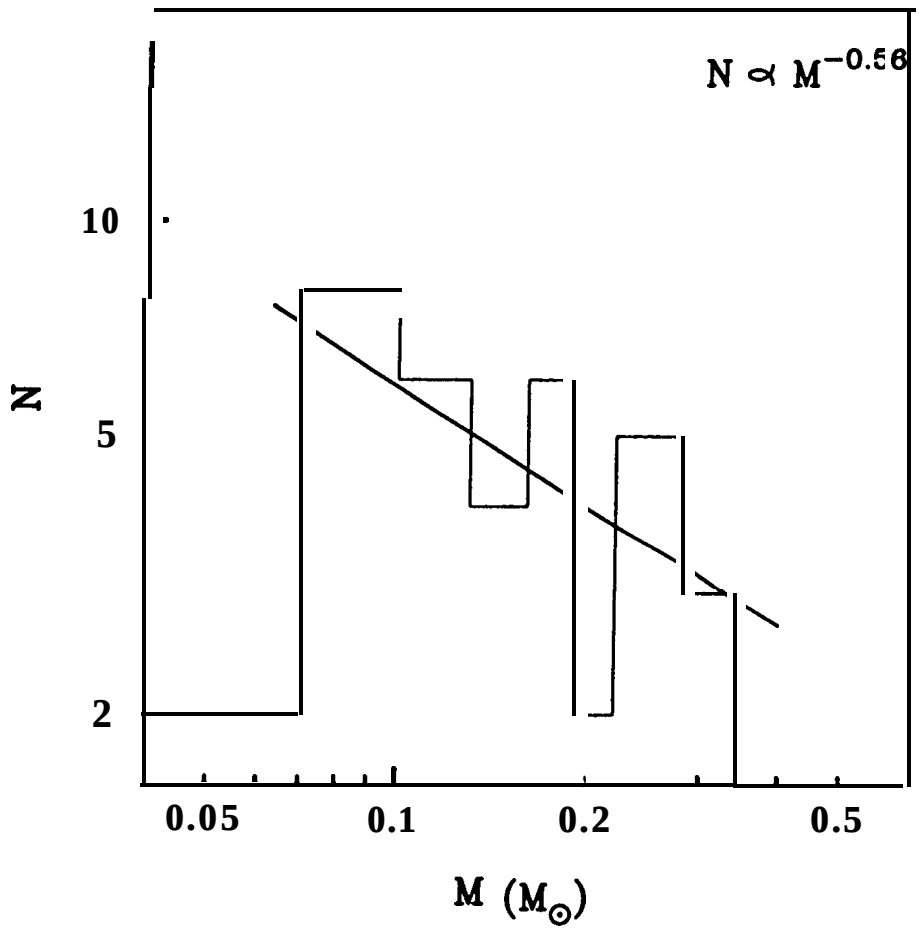

FIGURE 4

Low Mass Clumps in TMC-1: Scaling Laws in the Small Scale Regime

R. Peng, W. D. Langer, T. Velusamy, T. B. H. Kuiper, S. Levin
MS 169-506
Jet Propulsion Laboratory
California Institute of Technology
Pasadena, CA 91109

ABSTRACT

We present new observational data on the small scale structure of the Taurus Molecular Cloud 1 (TMC-1) in the regime of 0.02-0.04 pc and 0.04 -0.6 $M_\odot$. Our analysis is based on high resolution, high signal-to-noise, observations of an 8' x8' area centered on the "cyanopolyyne peak" in the SE part of the TMC-1 ridge. The observations were made in the CCS 22 GHz and 45 GHz transitions using NASA's Deep Space Network 70-m and 34-m telescopes at the Goldstone facility. The CCS emission in this region originates in three narrow components centered on LSR velocities of ~5.7, 5.9, and 6.1 km s^{-1}. These components each represent a separate cylindrical feature elongated along the ridge. Among the three velocity components we identified a total of 45 clumps with a typical CCS column density of ~ few x 10^{13} cm^{-2}, an H_2 density of ~ few x104 cm^{-3}, and a mass in the range of 0.04 to 0.6 $M_\odot$. The statistical properties of these small scale clumps are compared with those of the larger "NH_3 cores" in cold clouds and "CS cores" in the hotter Orion region. The CCS clumps in TMC- 1 are found to conform to the Larson's scaling laws (relating observed linewidth to clump size) derived from the larger cores down to the small scale regime (0.02 pc and 0.04 MO). These clumps represent a regime where microturbulence is small, amounting to ~10% of the thermal pressure inside a clump. Of the 45 clumps, only five appear to be gravitationally unstable to collapse. The 6.1 km s^{-1} component contains all the gravitationally unstable clumps and is the most likely site for future star formation.

Subject headings: ISM: clouds - ISM: individual (Taurus Molecular Cloud) - ISM: molecules - stars: formation - radio lines: ISM

1. Introduction

The mechanisms by which interstellar clouds produce the star forming cores is not well understood owing in part to the lack of sufficient data to draw a complete time line of the formation of these cores. Two such schemes have been proposed: gravitational fragmentation of larger structures or coalescence of smaller fragments formed from turbulent cascade. Larson (1981) found from a wide variety of molecular clouds an empirical correlation between the observed line width, cloud size, and the gas density, which was latter known as Larson's Laws. Although the physical basis of Larson's scaling laws is not well understood, the self-similar structure of molecular clouds as described by the Larson's Laws has been argued by many authors as turbulent in nature (see e.g. Goodman et al. 1997 and references therein).

In the cores of cold dense clouds there are many examples of line widths measured with trace molecules, such as CS, NH_3, HC_3N, that are narrower than the thermal line width of molecular hydrogen at 10 K (Fuller & Myers 1992, 1993, and Langer et al. 1995). In these cases the velocity field is mainly thermal and has a small non-thermal component which is probably due to microturbulent (subsonic) motions. Thermal H_2 pressure provides the main support for the cores. This situation is in contrast to cores in warmer molecular clouds where non-thermal components (likely macro-turbulence) dominate the velocity field as well as core support. These observations of small scale thermal features in cold dense clouds raise some important questions regarding the origin of the cold cores.

TMC-1 has been a prime object for studying cold cores because of its proximity and small velocity dispersion. To study the small scale structure of a quiescent dark cloud, such as TMC- 1, one needs to have sufficient spatial resolution, as well as high enough spectral resolution to sample molecular lines of thermal width (typically ~ 0.1 km s^{-1} for CCS in cold, dark clouds). There have been a number of studies of the structure of TMC-1 in a variety of tracers (e.g. Hirahara et al 1992, Onishi et al. 1996). Recently Langer and co-workers extended these studies to small scale structures through single-dish and interferometric observations of CS and CCS (Langer et al. 1995) and from multi–transition analysis of CCS (Wolkovitch et al. 1997). Using a heavy molecular tracer (CCS) with narrow thermal line-widths (~ 0.1 km s^{-1} at $\sim$ 10 K), Langer et al. (1995) have shown that little turbulence is seen in the small scale structures in TMC-1. Therefore the small scale clumps in TMC-1 can be used to study the behavior of the scaling laws down to smaller sizes and masses, in a regime of low turbulence, where the turbulent widths are ~ 0.1 km s^{-1}.

Here we present an extension of the earlier work by Langer et al. (1995) and Wolkovitch et al. (1997), consisting of better sampled and more extensive maps of CCS centered on the "cyanopolyyne peak" in the southeast part of the TMC-1 ridge. CCS is reasonably

abundant and widely distributed in TMC-1 (Hirahara et al. 1992, Langer et al, 1995, Wolkovitch et al. 1997), making it an excellent tracer for moderate density ($n(H_2) \gtrsim 10^4$ cm^{-3}) molecular gas.

From these high signal-to-noise, high spectral and spatial resolution maps we are able to identify more small scale clumps than seen in earlier work. The properties of these clumps are determined from an excitation analysis. The large number of clumps, 45 in total, makes it possible to evaluate their statistical properties and to test the Larson's scaling law in a small scale, low-mass regime. Of the 45 clumps identified in the area, only five are gravitationally unstable to collapse while the remainder are evenly split between unbound and stable objects. All the unstable clumps are associated with one spatial–velocity feature near the cyanopolyyne peak. Our results show that Larson's scaling laws extend down to the low mass clumps in TMC-1.

2. Observations and Data Reduction

Observations of the CCS 22 GHz and 45 GHz transitions were made with the Deep Space Network (DSN) 70-m and 34-m telescopes at the NASA Goldstone Facility over the period from April 1994 to March 1997. The 70-m telescope observations used a K-Band HEMT receiver tuned to the rest frequency of the CCS $J_N = 2_1 \rightarrow 1_0$ transition (22344.033 MHz). The system temperature is $\sim$70 K and the FWHM antenna beam is 45". Observations of the CCS $J_N = 4_3 \rightarrow 3_2$ transition (45379.033 MHz) using the 34-m beam waveguide telescope equipped with a Q-Band HEMT receiver were made with a typical system temperature of $\sim$130 K and a comparable FWHM beamwidth of 50". Both the 22 GHz and 45 GHz observations utilize the same backend, consisting of a Wide Band Spectrum Analyzer (WBSA; Quirk et al. 1988) covering a bandwidth of 40 MHz with over two million channels. We used a subset of 5 MHz in the middle of the WBSA for both the 22 GHz and 45 GHz observations, producing spectra of 8192 channels with a spectral resolution of 0.008 km s^{-1} and 0.004 kms-^{1}, respectively. The spectra were further smoothed to a resolution of 0.024 km s^{-1}.

Extensive mapping was made at the CCS 22 GHz transition over an area of 8' x8' centered on the cyanopolyyne peak of TMC-1 RA(1950) = $04^h38^m42^s.0$, DEC(1950) = $25°34'50''.0$, the Core D region of Hirahara et al. (1992), at a spacing of 25" (Nyquist sampled). Observations of the CCS 45 GHz transitions were made towards peaks of the clumps identified from the CCS 22 GHz maps (see section 3). Observations at both frequencies were conducted in a position switching mode with four on-positions between two adjacent off-positions. A 10-min on-source integration at 22 GHz yields a rms noise

level of ∼ 0.06 K at a resolution of 0.024 kms-^{1}, while a comparable rms noise level is achieved at 45 GHz with a 20-min on-source integration after smoothing the spectra to the same resolution.

Calibration of the antenna temperature for each observing session was made with a noise diode and an ambient load. Corrections for atmospheric emission and absorption, as well as antenna gain variations over elevation angles were made in a self-consistent fashion. A reference position (the cyanopolyyne peak) was observed once every hour during each track. Scaling factors were calculated by comparing these values to that obtained with the NRO 45-m telescope towards the same position (Suzuki et al. 1992, Hirahara et al. 1992). The spectra taken at other positions were then scaled accordingly. Standard spectral line operations, such as co-adding spectra taken at the same position and removal of linear baselines, were performed on all the spectra.

3. Results

All the CCS spectra show evidence of a complex line shape best explained by three velocity components (cf. Langer et al. 1995). We show in Figure 1 representative spectra of CCS at both 22 GHz and 45 GHz towards three different positions in the Core D region of TMC1. To extract the structure and gas properties of these features separately we fitted each spectrum with three gaussian profiles. The spectral decomposition is conducted as follow: one gaussian is fitted to each line wing of the observed profile, and is subsequently subtracted from the line profile; the remaining part is fitted with a third gaussian. An example of the spectral decomposition is shown in the middle panels of Figure 1, with dotted lines showing the gaussian fits and residuals plotted at the baseline level in solid lines. The velocities of the fitted gaussian components generally group around LSR velocities centered at 5.7, 5.9, and 6.1 km s^{-1}. The gaussian components have FWHM line widths in the range of 0.14 to 0.23 km s-l, as compared to 0.09 km s^{-1} for the thermal broadening of the CCS lines at 8 K.

3.1. Spatial–Velocity Distribution of 22-GHz CCS Emission

The distribution of CCS emission separates into three features each delineating an elongated structure oriented along the SE-NW direction. Figure 2 shows the distribution of integrated intensity of the three components. Molecular gas traced by the CCS 22 GHz transition largely follows that seen in other carbon-chain molecular line emission in the

TMC-1 ridge. All three components indicate little extension to the SE beyond the map, but in the NW there is clearly CCS emission beyond the mapped region extending towards the NH_3 peak in the northwest ridge. The 5.9 km s^{-1} component appears to trace a narrow strip along the "crest" of the TMC-1 ridge. Overall, maps of the three components have an elongated appearance along the ridge, which may represent a cylindrical structure for each component. Each one of the cylindrical components is very clumpy as can be seen in the individual maps in Figure 2,

We identified 45 clumps in the maps for the three velocity components. As marked in Figure 2, most of these are clearly evident by visual inspection. The high signal-to-noise ratio (> 20) of the spectra allows us to decompose even the few cases of significant spatial overlapping (e.g. b14 & 15; r9, 10 & 11). Following the methodology of CLUMPFIND (Williams et al. 1994), we trace out gaussian profiles for peaks above the 5σ level. Some areas clearly show significant overlapping of these gaussian clumps. In such cases, we carefully inspect the contour topology at relatively lower levels (i.e. at and around the half-maximum level) to examine the number and size of gaussian components that will fit into the contour envelope. Each clump is characterized by its peak position and the major and minor axes of the FWHM area. The clumps are marked in Figure 2 and listed in Table 1. Clumps are grouped in Table 1 by their velocity, with the designation: b (blue), m (middle), and r (red) refer to the 5.7, 5,9, and 6.1 km s^{-1} velocity features, respectively. The clumps are numbered along the ridge from NW to SE. The position of each clump is shown in the second and third column of Table 1 as offsets in RA and Dec. to the reference position, $RA(1950) = 04^h38^m42^s.0, Dec(1950) = 25°34'50''.0$ (CCS peak). The table also lists the major and minor axial size, the peak brightness temperature T_R, center velocity v_{LSR}, and the FWHM line width w of the CCS 22 GHz spectrum determined at the peak of each clump.

3.2. H_2 Density and CCS Column Density

From the peak brightness temperature T_R at 22 and 45 GHz we derive the gas density and CCS fractional abundance in the individual clumps using an excitational analysis. The CCS model calculations of Wolkovitch et al. (1997) were used with a fixed kinetic temperature of 8 K, which appears representative for the SE part of the TMC-1 ridge. The values of $X/(dv/dr)$, the ratio of CCS fractional abundance (X), and the velocity gradient across the cloud (dv/dr) were obtained from the LVG calculations. We find $X/(dv/dr)$ to be tightly clustered for clumps within each cylindrical component (see Table 2), indicating a roughly constant CCS fractional abundance for each component. This result allows us

to simplify derivations of CCS column density and mass by adopting an average value of $X/(dv/dr)$ for all clumps, and deriving the H_2 density $(n(H_2))$ for each clump using only the T_R at 22 GHz, $N_{CCS} \sim n_{H_2}(X/(dv/dr))\Delta v$ cm^{-2}. The results are listed in Table 1.

3.3. Clump Mass

The mass of each clump is

$$M \sim 1.15 \times 10^{-26} N_{H_2} b_{maj} b_{min} \ M_\odot \quad (1)$$

where b_{maj} and b_{min} are the major and minor axes of the FWHM size of the clump in arcsecond; N_{H_2} is the H_2 column density toward the clump. Equation (4) includes the contribution from helium assuming a fractional abundance of 0.1 relative to hydrogen nuclei. N_{H_2} is derived from

$$N_{H_2} \sim \frac{\mathrm{Nets}}{X}. \quad (2)$$

We used the average fractional abundance, (X), for the three velocity features as given in Table 2. The clump masses are listed in Table 1.

4. Discussion

TMC-1 has been well studied because of its unique morphology and chemical inhomogeneities. Many interesting models have been proposed to explain these aspects of the cloud, for example, cloud collision (Little et al. 1978) and sequential star formation along the ridge (Hanawa, Yamamoto, & Hirahara 1994). In this paper we will not attempt to interpret the chemical and physical properties of the TMC-1 ridge, but restrict our discussion to the new observational data on the small scale clumps in the SE part of the ridge as traced by CCS.

4.1. Statistical Properties of the CCS Clumps

What are these low mass clumps in TMC-1 as traced by the CCS emissions and what is their significance to star formation? To answer these questions, it is important to compare the physical characteristics of these clumps with those of the other star forming cores such as the cold cloud "NH_3 cores" of Benson & Myers (1989) and the hotter CS cores in Orion-A (Tatematsu et al. 1993). In Figure 3 we plot in logarithmic scale the observed FWHM line widths versus mass and radius of all clumps and cores.

In the left panel of Figure3 we show the plot of line width versus clump mass. The thick dashed line in the figure represents a power law fit of the form: $\Delta V_{obs} \propto Ma$ where $\alpha = 0.23$ is the fit for the Orion-A CS cores by Tatematsu et al. (1992). The Orion-A CS cores are generally in virial equilibrium, and non-thermal pressure provides the main support in a core, judging from the observed line width in comparison with the estimated thermal broadening of molecular hydrogen. Clearly, dense cores in cold dark clouds follow a different power law. For the NH_3 cores and small scale CCS clumps, we find

$$\Delta V_{obs} \sim 0.22 M^{0.14} \quad (3)$$

where the linear correlation coefficient is 0.79. The fit is shown as a thick dotted line. The different linewidth versus mass relation for the dark cloud cores and small scale clumps may reflect the fact that non-thermal pressure plays a substantially smaller role in supporting the cores compared to their counterparts in Giant Molecular Clouds (GMC'S). In addition, there is an increasing proportion of small scale clumps departing from virial equilibrium as one moves into the small scale regime in dark molecular clouds (see Section 4.2).

In the right panel of Figure 3 we show the plot of observed line width versus size of cores and clumps. The thick dashed line in the right panel shows Larson's Laws (Larson 1981) as applied to dense cores in Orion-A, $\Delta V_{obs} \sim 2.5 R^{0.4}$, from Tatematsu et al. (1992). We also fit the NH_3 cores and CCS clumps in dark clouds with a power law,

$$\Delta V_{obs} \sim 0.69 R^{0.39} \quad (4)$$

where the linear correlation coefficient is 0.87. The fit is shown as a thick dotted line. It agrees with those derived for dark cloud cores by Fuller & Myers (1992) with a power index of 0.4 and 0.44 for cores with and without stars, respectively. The plot clearly shows that Larson's Law still hold for structures in dark clouds down to a scale of ~ 0.02 pc.

The result that the same scaling law applies to dense cores in both GMC'S and cold dark clouds implies that these two kinds of clouds share the same mechanism of fragmentation, either turbulent cascade or gravitational fragmentation, or both. It is also evident that GMC'S and dark clouds have different velocity dispersion coefficients in the Larson's Laws (2.5 and 0.69, respectively). This variation is an indication of the different energy content in the cascading structures in GMC'S and dark clouds, with GMC'S being more energetic.

With a sizable number of clumps identified around the cyanopolyyne peak in the SE region of TMC-1, we can also study the mass distribution of clumps in the low-mass regime. In Figure 4 we plot the number of clumps at each mass interval and fit it with a power law,

$$N \sim 1.6 M^{-0.56} \quad (5)$$

which is shown as a solid line in the figure. The corresponding mass spectrum index dN/dM = –1 .56 is in good agreement with those obtained for cores of large mass (M $\gtrsim$ 20 $M_\odot$) in various GMC's ($\sim$ – 1.6, see Blitz 1991 and references therein). This compares to a mass spectrum index of –1.2 for dark cloud cores of Myers, Linke, & Benson (1983) and –0.9 for $C^{18}O$ cores in Taurus molecular cloud (Onishi et al. 1996). Onishi et al. argued for a flatter mass spectrum in the low mass range, which does not appear to bear out in our results for the CCS clumps with masses typically smaller than 0.5 $M_\odot$.

4.2. **Dynamical Status of the CCS Clumps**

To assess the dynamical status of each clump with regard to gravitational collapse, we calculate the virial mass for each clump in two limiting cases (MacLaren et al. 1988):

$$M_{vir} \sim \gamma R (\Delta v_{av})^2 \ M_\odot \qquad (6)$$

where $\gamma \sim 210$ for constant density distribution, and 7- 126 for r^{-2} density distribution in the clump. R is the average radius of the clump listed in Table 1, and is calculated by

$$R \sim 4.07 \times \sqrt{b_{maj} b_{min}} \cdot pc, \qquad (7)$$

where b_{maj} and b_{min} are the major axes of the clump in arcsec. A distance of 140 pc is used for TMC-1 in the above calculation. Δv_{avg} is the line width of the average (mainly H_2) gas of the clump,

$$\Delta v_{avg} = 2.35 \sqrt{\sigma^2_{turb} + \sigma^2_{therm}(H_2)} \qquad (8)$$

where

$$\sigma_{therm} = 0.0912 \sqrt{\frac{T_K}{m_{mau}}} \ km\ S\text{-}l \qquad (9)$$

and m_{mau} = 2.3 for average gas. The velocity dispersion resulting from turbulent motions in the clump, σ_{turb}, is obtained using the measured line width and the thermal dispersion of CCS with m_{mau}= 56:

$$\Delta v_{obs} = 2.35 \sqrt{\sigma^2_{turb} + \sigma^2_{therm}(CCS)}. \qquad (10)$$

Two estimates of M_{vir} for each clump are listed in Table 1, depending on the assumed density profile.

Clearly, a clump is more prone to gravitational collapse if it has a centrally condensed structure rather than a uniform density profile, as the viral mass in the first case is substantially smaller. When M > M_{vir}, a clump is gravitationally unstable, and is likely to collapse. If 0.5 M_{vir} < M < M_{vir}, it is stable. If M <0.5 M_{vir}, a clump is gravitationally

unbound. We use the notation "BC", "S", and "UB" in Table 1 to represent the three cases of being bound and capable of collapse, stable, and unbound. Of the 45 clumps, 19 appear to be gravitationally unbound; 21 are stable and only five are likely to collapse under their own gravity. If the clump mass is compared against the virial mass of a uniform clump, then all the clumps in the 5.7 km s^{-1} component and most of those in the 5.9 km s^{-1} component would become gravitationally unbound, and all the clumps in the 6.1 km s^{-1} component would be stable.

It is interesting to note that the 6.1 km s^{-1} component contains all the clumps that are likely to undergo gravitational collapse. This suggests that it is in a relatively more advanced evolutionary stage than the other velocity components. It also corroborates the fact that high resolution VLA observations of a portion of the region (Langer et al. 1995 and Velusamy 1997) see only condensations in the 6.1 km s^{-1} component. Clearly, the 6.1 km s^{-1} component is the most likely center of future star forming activity in the region. Note that all five candidates for core collapse have masses in the range of 0.5-0.6 $M_{\odot}$, indicating a future population of low mass stars.

It is also interesting that at least 19 (and perhaps up to 30) out of 45 clumps in the region are gravitationally unbound. Such a finding comes as no surprise because this region in the TMC- 1 ridge indeed lacks star forming activity. Previous studies of cores in the TMC-1 ridge with coarser spectral and spatial resolutions (e.g. Hirahara et al. 1992 and Onishi et al. 1996) generally find fewer but larger cores all of which appear to be gravitationally bound. One of these cores, Core D, (Hirahara et al. 1992) is now resolved into 45 small clumps. Among them a substantial portion are gravitationally unbound. This result may indicate a break down of the self-similar structure of molecular clouds (Falgarone, Phillips, & Walker 1991) as one probes the physical regime where thermal pressure inside a clump is dominant over that of non-thermal pressure (by a factor of ~ 10 for the CCS clumps).

The unbound clumps, if not confined by an external pressure, would disperse at the sound speed of ~ 0.3 km s^{-1} over a time scale of $\sim$ 2x105 yr, which compares to a molecular cloud's lifetime of $\gtrsim 10^6$ yr. As gravitationally unbound clumps appear in such a large proportion, they cannot all be transient in nature. We suggest that thermal and turbulent pressures of the interclump gas may contribute to keep these clumps pressure-bound.

To estimate the external pressure required to confine an unbound clump, we calculated the virial parameter (Bertoldi & McKee 1992) for each clump:

$$\alpha = \frac{5\sigma_{av}^2 R}{GM}. \qquad (11)$$

This parameter measures the relative importance of internal kinetic energy and the

gravitational potential, and is within afactorof 1 to 1.3 of the ratio of internal kinetic energy and gravitational potential of the clump. Assume the clumps are in a quasi-virial equilibrium whereby the internal kinetic energy is in balance with the gravitational potential and the surface energy exerted by ambient gas pressure. We can estimate the temperature of the interclump gas T_{ic} required to confine the clumps if the external pressure is only of thermal origin:

$$T_{ic} = (1 - \frac{a}{\alpha})\frac{n_{cl}}{n_{ic}} T_{cl}\ K \qquad (12)$$

where the factor *a* ranges between 1 and 1.3, n_{ic} is the gas density of the interclump gas, n_{cl} and T_{cl} are the gas density and kinetic temperature of the clump, respectively.

For the unbound clumps listed in Table 1, the virial parameter ranges between 5.6 to 17.9 with a median value of ~9.5. The interclump gas probably has a density of ~2 x 10^3 cm^{-3} as seen in $C^{18}O$ emission of the region (Langer et al. 1995). With a clump temperature of 8 K and a clump density of ~10^4 cm^{-3}, the interclump gas would need to have a temperature of ~ 40 K to confine the clumps with thermal pressure. Such a temperature appears to be too high by at least a factor of two than the interclump gas temperature as estimated from the $C^{18}O$ observation. On the other hand, microturbulence in the interclump gas may provide enough pressure to confine the clumps. The $C^{18}O$ observations of the region (Langer et al. 1995) shows a typical line width of 0.45 km s^{-1}, within which the thermal broadening accounts for only ~1/4 of the line width. The remaining part would be due to microturbulence in the interclump gas, which would have a turbulent pressure equivalent to the thermal pressure at a gas temperature of 75 K to 100 K, enough to confine the unbound clumps.

4.3. Relative Motion Among CCS Clumps

The high spectral resolution and the high signal-to-noise ratio obtained for the CCS spectra enable us to determine the clump velocities to a high degree of precision and hence to study the relative movement among the clumps within each of the three cylindrical features in the TMC-1 ridge. As seen in Tables 1 and 2, the velocities of the clumps in each feature have a small dispersion about the mean with a standard deviation of 0.03 km s-l. This amounts to a random motion among the clumps of the order 0.05 km s-l, assuming an isotropic random velocity distribution, At such a small relative velocity, it would take ≳2.4 x106 yr for a clump to migrate across the ridge of* 3' (~0.12 pc) in width, and four to five times longer to travel from one end to the other along the ridge.

It is interesting to compare the above crossing time with the collision time over which a

clump is likely to encounter another clump in the same cylindrical component. To calculate the collision time, we estimate the average separation between clumps as

$$\Delta l \sim 2(\frac{1}{\sqrt[3]{\gamma}} - 1)r, \quad (13)$$

where r is the clump radius, and γ is the clump filling factor in each component. γ is estimated by:

$$\gamma \sim \frac{n_{clump} V_{clump}}{V_{Comp}}, \quad (14)$$

where n_{clump} is the number of clumps in the cylindrical component, V_{clump} is the average volume of each clump, and V_{comp} is the volume of the component. Assuming a cylindrical geometry for the component and spherical geometry for the clumps, the clump filling factor is estimated to be 0.11, 0.19, and 0.07 for the 5.7, 5.9 and 6.1 km s^{-1} features, respectively. The average separation Al is then $\sim$0.07, 0.04, and 0.08 pc, respectively, and the corresponding collision time is 1.3x106, 8.9x105, and 1.7x106 yr.

Comparing different time scales (τ(dispersion) $\sim$ 2x 10^5 yr, τ(collision) $\sim$ 1x 10^6 yr, and τ(crossing) > 2x106 yr), it would seem that a CCS clump is more likely to be subject to merging or fragmenting due to collisions with other clumps rather than traveling intact along the ridge. On the other hand, clumps do move around appreciably within each cylindrical component over their lifetime, providing sufficient mixing for a homogeneous temperature and chemical abundance distribution in each cylindrical component.

4.4. Comparison of the Three Velocity Features

We list in Table 2 the average values of $v_{LSR}, w, dv/dr, n_{H_2}$, and N_{CCS} for the clumps in each velocity component. The associated errors are standard deviations. Also listed are average values of $\log(X/(dv/dr))$ and X. The error associated with $\log(X/(dv/dr))$ reflects the scatter of the clump distribution on a $\log(n_{H_2})$ versus $\log(X/(dv/dr))$ plot, the error for X is the compound error of $\log(X/(dv/dr))$ and (dv/dr). The total mass of molecular gas traced by CCS in each cylindrical component is also given in the table. We summarize in Table 2 the total number of bound and unbound clumps in each velocity feature.

As seen in Figure 2, the components have a different overall structure in the CCS emission, The 5.7 km s^{-1} component is the most extended among the three. It also has on average a broader CCS line width and a markedly higher CCS fractional abundance than the other two (see Table 2). A higher CCS abundance has been related to young dense material in dynamical models (Kuiper et al. 1996; Bergin & langer 1997). In addition,

the predominance of the unbound clumps in the 5.7 and 5.9 km s^{-1} features is consistent with the interpretation that they trace gas at a relatively younger evolutionary phase than the 6.1 km s^{-1} feature. Overall, the 5.7 km s^{-1} component seems to be a loosely structured cloud with relatively new gas of moderate density. The 6.1 km s^{-1} component, in comparison, appears more evolved with a tightly confined structure.

5. Conclusion

We have mapped an 8' x8' area around the cyanopolyyne peak in the nearby dark cloud TMC-1 in the CCS 22 GHz transition with Nyquist sampling and a 0,008 km s^{-1} velocity resolution. We combined this map with observations of the CCS 45 GHz transition to analyze its small scale structure. The region contains three major cylindrical features at LSR velocities of 5.7, 5.9 and 6.1 $km\,s^{-1}$. The 5.7 $km\,s^{-1}$ cloud and the 6.1 km s^{-1} components occupy similar areas in the sky along the TMC-1 ridge, while the 5.9 km s^{-1} component is more spatially confined,

Using a multi-gaussian spectral decomposition and spatial-spatial maps we identified 45 clumps in the three velocity components. Most of the clump masses range from 0.1 to 0.5 $M_\odot$, while a few are much smaller, $\sim 0.05\,M_\odot$. The CCS line width of the clumps ranges from 0.14 to 0.23 km s^{-1}, with microturbulence in the clump contributing $\sim$ 1/4 of the H_2 line broadening.

The CCS clumps in TMC-1 indicate that Larson's scaling laws still hold in the small scale regime down to 0.02 pc and 0.04 $M_\odot$.

Out of the 45 clumps, only five are likely to be gravitationally unstable to collapse. The rest are stable or unbound and the predominance of these clumps is consistent with the low star forming activity in this region of the TMC-1 cloud.

R. P. is a National Research Council Research Associate at the Jet Propulsion Laboratory, California Institute of Technology. This research was conducted at the Jet Propulsion Laboratory, California Institute of Technology under support from the National Aeronautics and Space Administration. We would also like to thank the DSN operations staff for their assistance with the observations.

TABLE 1

CCS CLUMPS IN TMC-1 CORE D REGION

Clump[a]	Offset[b] arcsec	Size[c] arcsec	T_R K	V_{peak} km/s	w km/s	n_{H_2}[d] cm^{-3}	N_{CCS}[d] cm^{-2}	M[d] MO	M_{vir}[e] $M_\odot$	Note[f]
b1	–140, 235	**86×76**	**2.0**	5.768	0.211	7.6(3)	1.6(13)	0.12	0.640.38	**UB**
b2	-136,181	83x61	**2.1**	5.738	0.194	8.3(3)	1.6(13)	0.09	0.560.34	**UB**
b3	-106,161	89x67	2,4	5.750	0.184	9.8(3)	1.8(13)	0.13	0.610.36	**UB**
b4	-141,124	91x69	3.4	5.701	0.186	1.8(4)	3.3(13)	0.24	0.620.37	S
b5	-104,100	**89×80**	3.1	5.714	0.216	1.5(4)	3.2(13)	0.27	0.660.40	s
b6	-75, 84	70x61	**2.9**	5.696	0.211	1.3(4)	2.7(13)	0.14	0.520.31	**UB**
b7	-50, 55	86X61	3.0	5.693	0.205	1.5(4)	3.0(13)	0.19	0.570.34	s
b8	–107, 41	84X 70	3.3	5.681	0.232	1.7(4)	3.8(13)	0.27	0.610.36	S
b9	-80, 24	**89×73**	3.4	5.676	0.217	1.8(4)	3.8(13)	0.30	0.630.38	S
b10	–49, 16	86x 70	3.6	5.705	0.194	2.0(4)	3.8(13)	0.27	0.61 0.37	S
b11	3,-1o	80X 68	3.5	5.713	0,162	1.8(4)	2.8(13)	0.18	0.580,35	S
b12	9,-52	83 x64	3.7	5.705	0.160	2.1(4)	3.3(13)	0.21	0.570.34	s
b13	-53,-78	67x56	2.0	5.654	0.216	7.6(3)	1.6(13)	0.07	0.480.29	**UB**
b14	41,-85	89X 64	3.3	5.711	0.156	1.7(4)	2.6(13)	0.18	0.590.36	S
b15	48,-115	89X 63	3.2	5.685	0.152	1.7(4)	2,5(13)	0.17	0.590.35	**UB**
b16	81,-149	86x 79	2.9	5.670	0.163	1.4(4)	2.2(13)	0.18	0.650.39	**UB**
b17	124,-185	92x61	**2.5**	5.656	0.203	1.1(4)	2.2(13)	0.15	0.590.35	**UB**
m1	-212,232	67x56	2.8	5.869	0.162	3.5(4)	1.7(13)	0.25	0.480.29	S
m2	– 176,164	83 x63	1.8	5.929	**0.169**	1.8(4)	9.4(12)	0.18	0.570.34	s
m3	-150,104	69x52	1.3	5.908	0.169	1.1(4)	5.7(12)	0.08	0.470.28	**UB**
m4	-80, 84	68x 59	1.0	5.864	0.180	8.9(3)	4.9(12)	0.07	0.500.30	**UB**
m5	-120, 74	67x52	1.2	5.855	0.176	1.1(4)	6.0(12)	0.08	0.470.28	**UB**
m6	–117, 39	61x49	0.9	5.832	0,161	7.2(3)	3.6(12)	0.04	0.430.26	**UB**
m7	–76, 26	70x61	1.2	5.856	0.171	1.1(4)	5.8(12)	0.09	0.520.31	**UB**
m8	-40, -3	89x57	1.4	5.879	0.166	1.3(4)	6.7(12)	0.13	0.560.34	**UB**
m9	**9,** -8	73x61	1.9	5.880	0.156	2,0(4)	9.6(12)	0.16	0.530.32	S
m10	12,–53	75x67	2,5	5.888	0.145	3.1(4)	1.4(13)	0.26	0,560.34	S
m11	35,–84	70x 53	1.9	5.907	0.155	2.0(4)	9.6(12)	0.14	0.480.29	**UB**
m12	0,-109	76X 50	1.5	5.886	0.156	1.4(4)	6.7(12)	0.10	0.490.29	**UB**
m 13	46,-140	80x53	1.2	5.936	0.163	1.1(4)	5.5(12)	0.09	0.510.31	**UB**
m14	99,-180	89 x69	1.3	5.929	0.139	1.2(4)	5.2(12)	0.12	0.620.37	**UB**
m15	128,-196	73x 56	0.9	5.903	0.153	8.1(3)	3.8(12)	0.06	0.500.30	**UB**
r1	-112,235	92x64	1.8	6.105	0.177	3.0(4)	1.0(13)	0.40	0.600.36	BC
r2	–80, 181	97x 68	**1.6**	6.090	0.172	2.4(4)	8.0(12)	0.35	0.640.38	S
r3	–121, 142	82X 76	1.7	6.004	0.161	2.6(4)	8.1(12)	0.34	0.620.37	S
r4	-76,121	86X61	2.0	6.067	0.147	3.4(4)	9.7(12)	0.34	0.570.34	**BC**
r5	-33, **95**	78X 63	**1.9**	6.074	0.149	3.3(4)	9.6(12)	0.31	0.550.33	s
r6	-109, 61	58x52	1.4	6.003	0.178	2.1(4)	7.3(12)	0.15	0,440.26	S
r7	-10, 52	83X 76	2.4	6.084	0.169	4.5(4)	1.5(13)	0.62	0.630.38	**BC**
r8	-46, 21	86 x63	1.8	6.072	0.165	2.9(4)	9.3(12)	0.33	0.580.35	S
r9	6, -7	73x55	2.1	6.054	0.151	3.7(4)	1.1(13)	0.29	0.500.30	s
r10	28,-35	86X 64	2.()	6.040	0.160	3.5(4)	1.1(13)	0.40	0.580.35	**BC**
r11	3,-36	70 x67	2.3	6.044	**0.149**	4.4(4)	1.3(13)	0.40	0.540.33	**BC**
r12	70.–93	75x **56**	**1.9**	**6.010**	0.142	3.3(4)	9.1(12)	**0.26**	0.51 0.31	s
r13	27.-106	76x52	1.6	**6.008**	**0.159**	2.5(4)	7.7(12)	**0.20**	0.50 **0.30**	s

[a] Letters b (blue), m (middle), and r (red) refer to the 5,7, 5.9, and 6.1 km s^{-1} components, respectively.

[b] Peak offsets in arcsecond relative to RA(1950) $04^h38^m42^s.0$, Dec(1950) $25°34'50''.0$

[c] Major and minor axes (arcsecond) of the FWHM clump area

[d] Numbers in parentheses are exponents to H_2 density and CCS column density

[e] Virial masses for density distribution of the form: $\rho \sim r^a$, where $a=0,-2$ respectively.

[f] UB: unbound; S: stable and hound; BC: bound and unstable, likely to collapse.

TABLE 2

AVERAGE PROPERTIES OF THE THREE CCS COMPONENTS IN TMC–1 CORE D REGION

Layer	$\langle V_{peak}\rangle$[a] km/s	$\langle w\rangle$[a] km/s	$\langle \mathcal{X}\rangle$[b]	$\langle dv/dr\rangle$[c] km/s/pc	$\langle X\rangle$[d] $\times 10^{-9}$	$\langle n_{H_2}\rangle$ $\times 10^{4}$	$\langle N_{CCS}\rangle$ $\times 10^{12}$	M	B/U MO	[e]
5.7 km/s	5.70±0.03	0.19±0.02	−8.5±0.2	3.1±0.5	9.8±4.8	1.4±0.5	26.9±7.6	3.16		9/8
5.9 km/s	5.89±0.03	0.16±0.01	−9.0±0.2	3.1±0.4	3.1±1.5	1.5±0.8	7.6±3.7	1.85		4/11
6.1 km/s	6.05±0.03	0.16±0.01	−9.2±0.1	2.8±0.4	1.8±0.5	3.2±0.7	9.9±2.0	4.39		13/0

[a] Average peak velocity and line width of the CCS 22 GHz transition in each component

[b] Average and scatter of $\mathcal{X}(=\log(X/(dv/dr))$ found from fitting the clumps to LVG calculations

[c] **Average velocity gradient for each component**

[d] CCS fractional abundance for each component with compound errors of X and (dv/dr)

[e] The number of gravitationally bound and unbound clumps in each component

REFERENCES

Bergin, E. A., &Langer, W. D. 1997, ApJ, in press

Benson, P. J. & Myers, P. C. 1989, ApJS, 71, 89.

Bertoldi, F. & McKee, C. F. 1992, ApJ, 395, 140.

Blitz, L., 1991, in The Physics of Star Formation and Early Stellar Evolution, eds. C. J. Lada & N. D. Kylafis (Dordrech: Kluwer)

Falgarone, E., Phillips, T. & Walker, C. K. 1991, ApJ, 378, 186.

Fuller, G. & Myers, P. C. 1992, ApJ, 384, 523.

Fuller, G. & Myers, P. C. 1993, ApJ, 418, 272.

Goodman, A. A., Barranco, J. A., Wilner, D. J.& Hyers, M.H. 1997, ApJ, submitted

Hanawa, T., Yamamoto, S. & Hirahara, Y. 1994, ApJ, 420, 318.

Hirahara, Y., Suzuki, H., Yamamoto, S., Kawaguchi, K. & Kaifu, N. 1992, ApJ, 394, 539.

Kuiper, T. B. H., Langer, W. D., Velusamy, T. 1996, ApJ, 468, 761.

Langer, W. D., Velusamy, T., Kuiper, T. B. H., Levin, S., Olsen E., & Migenes, V. 1995, ApJ, 453, 293.

Little, L. T., Riley, P. W., Macdonald, G. H., & Matheson, D. N. 1978, MNRAS, 183, 805.

MacLaren, I., Richardson, K. M. & Wolfendale, A. W. 1988, ApJ, 333, 821.

Myers, P. C., Linke, R. A. & Benson, P. J. 1983, ApJ, 264, 517.

Onishi, T., Mizuno, A., Kamura, A., Ogawa, H. & Fukui, Y. 1996, ApJ, 465, 815.

Quirk, M. P., Wilk, M. F., Garyantes, M. F. & Grimm, M. J. 1988, IEEE Trans. on Acoustics, Speech & Signal Processing, 36, 1854.

Suzuki, H., Yamamoto, S., Ohishi, M., Kaifu, N., Ishikawa, S., Hirahara, Y. & Takano, S. 1992, ApJ, 392, 551.

Tatematsu, K., Umemoto, T., Kameya, O., Hirano, N., Hasegawa, T., Hayashi, M., Iwata, T., Kaifu, N., Mikami, H., Murata, Y., Nakano, M., Nakano, T., Ohashi, N., Sunada, K., Takaba, H. & Yamamoto, S., 1993, ApJ, 404, 643.

Velusamy, T. 1997, private communication.

Williams, J. P., de Geus, E., Blitz, L. 1994, ApJ, 428, 693

Wolkovitch, D., Langer, W. D., Goldsmith, P. F. & Heyer, M. 1997, ApJ, 477, 241.

This preprint was prepared with the AAS LaTeX macros v4.0.

Fig. l. —Representative spectra of CCS at 22 GHz (top row) and 45 GHz (bottom row) towards three offset positionsin the SE region of TMC-1. Numbers in parentheses in the upper right corner of the top panels refer to the positional offset of the column in arcmin to the reference position at $\mathrm{RA}(1950) = 04^h38^m42^s.0, \mathrm{Dec}(1950) = 25°34'50''.0$. The spectra are sampled at a velocity resolution of 0.004 and 0.008 km s^{-1} at 45 GHz and 22 GHz respectively, and are smoothed to 0.024 km s-l. The spectra show underlying narrow-line structures, representing at least three gas components along the line of sight. Spectral decomposition (see text) is demonstrated using the (O, O) spectra shown in the middle panels. The gaussian fits are shown in dotted lines, and residuals in solid lines at the baseline level,

Fig. 2.— Distributions of integrated CCS line intensity of the three velocity components in the Core D region around the cyanopolyyne peak in TMC-1. The central velocity of each component is shown in the top-left corner of each panel; the filled circle in the lower-right corner of the bottom panel shows the FWHM beam of the telescope. Contours represent fractional levels in the range of 15% to 99% of the peak of each map (0.87, 0.39, and 0.42 K km s^{-1} for the 5.7, 5.9 and 6.1 km s^{-1} components, respectively) with an increment of 5%. The gray scale reflects the same intensity range. Labels mark the clumps identified in each map.

Fig. 3.— CCS clumps in TMC-1 Core D region (as filled triangles, squares and circles) in the logarithmic plots observed line width versus clump mass (left panel) and clump radius (right panel). A sample of NH_3 cores in dark clouds (Benson & Myers 1989) and the CS cores in Orion A molecular cloud (Tatematsu et al. 1992) are also plotted for comparison as open diamonds and filled stars, respectively. The two horizontal dashed lines mark the sound speed (V_c) at 8 K and the thermal broadening of CCS molecule $(\Delta V_t(\mathrm{CCS}))$ at 8 K. The thick dashed line in the left panel shows a power law fit of $\Delta V_{obs} \sim 0.43 M^{0.23}$ for the Orion-A CS cores; the thick dotted line shows the fit for dark cloud NH_3 cores and TMC-1 CCS clumps $(\Delta V_{obs} \sim 0.22 M^{0.14})$. Similarly, the thick dashed line in the right panel represent Larson's scaling laws applied to the Orion-A CS cores $(\Delta V_{obs} \sim 2.5\, R^{0.4})$ and the thick dotted line shows the fit to the dark cloud cores and CCS clumps $(\Delta V_{obs} \sim 0.69 R^{0.39})$.

Fig. 4.— Mass distribution function of CCS clumps in TMC-1 Core D region shown as a histogram. The solid line represents the least-square fit of the mass distribution function.

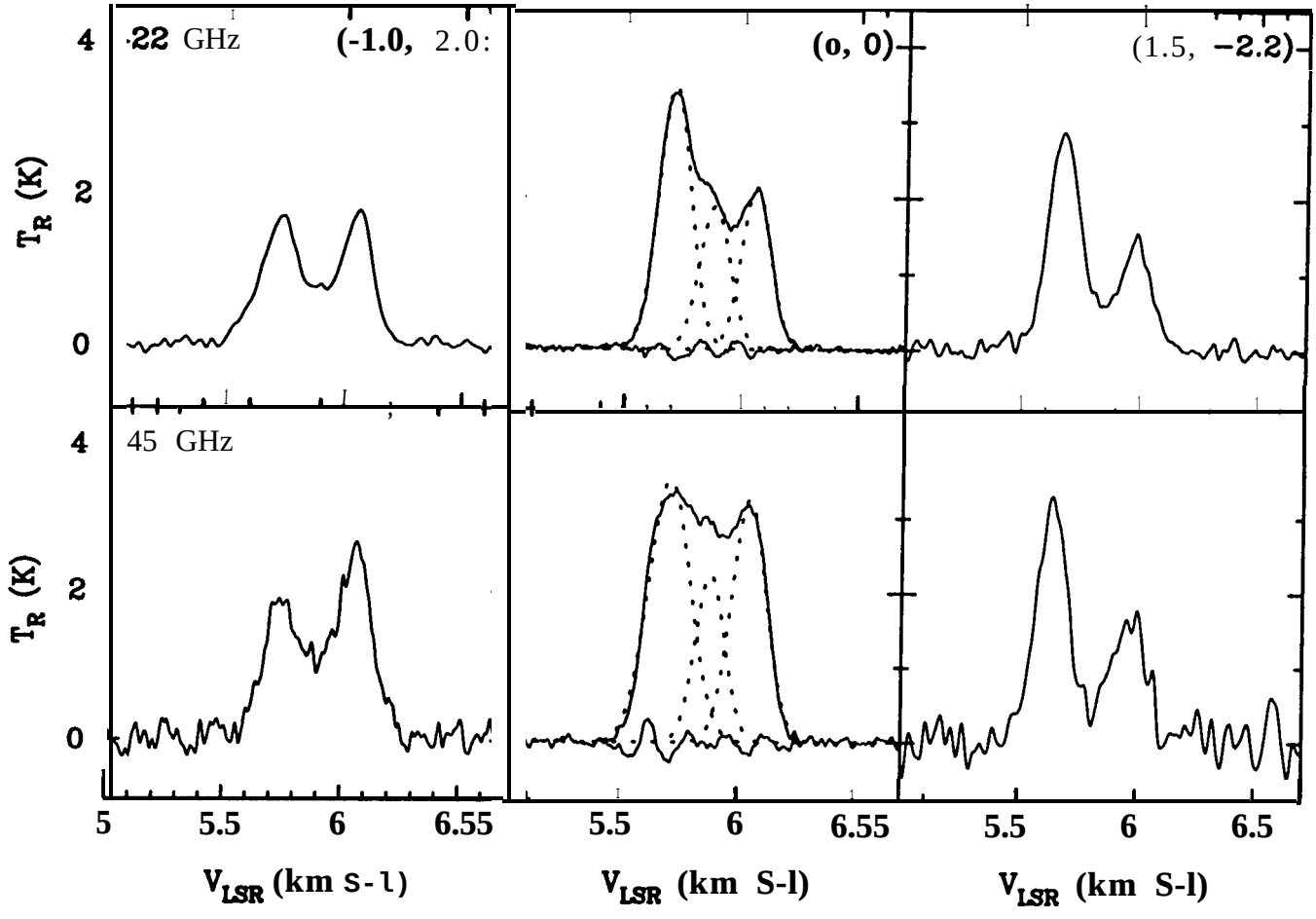

FIGURE 1

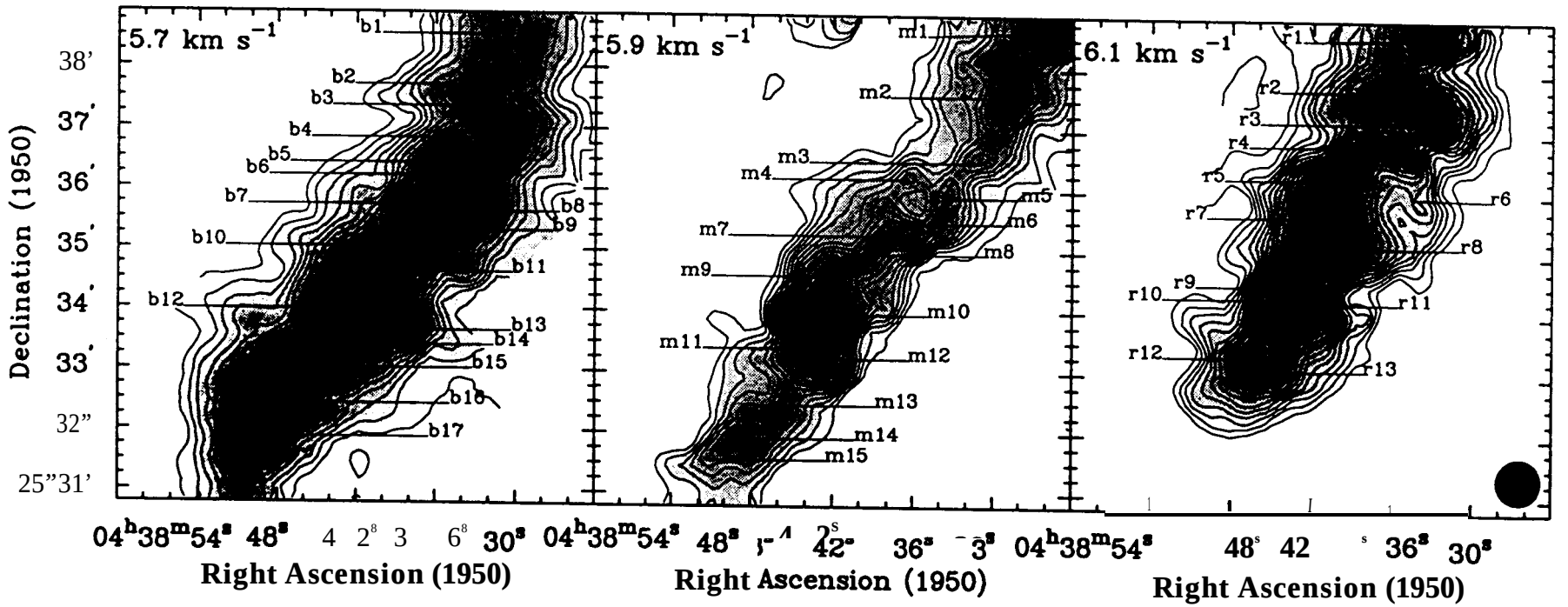
5.7 km s^{-1}
5.9 km s^{-1}
6.1 km s^{-1}
b1
b2
b3
b4
b5
b6
b7
b8
b9
b10
b11
b12
b13
b14
b15
b16
b17
m1
m2
m3
m4
m5
m6
m7
m8
m9
m10
m11
m12
m13
m14
m15
r1
r2
r3
r4
r5
r6
r7
r8
r9
r10
r11
r12
r13
Declination (1950)
38'
37'
36'
35'
34'
33'
32"
25"31'
04^{h}38^{m}54^s 48^s 4 2^s 3 6^s 30^s
04^{h}38^{m}54^s 48^s 42^s 36^s 30^s
04^{h}38^{m}54^s 48^s 42^s 36^s 30^s
Right Ascension (1950)
Right Ascension (1950)
Right Ascension (1950)

FIGURE 2

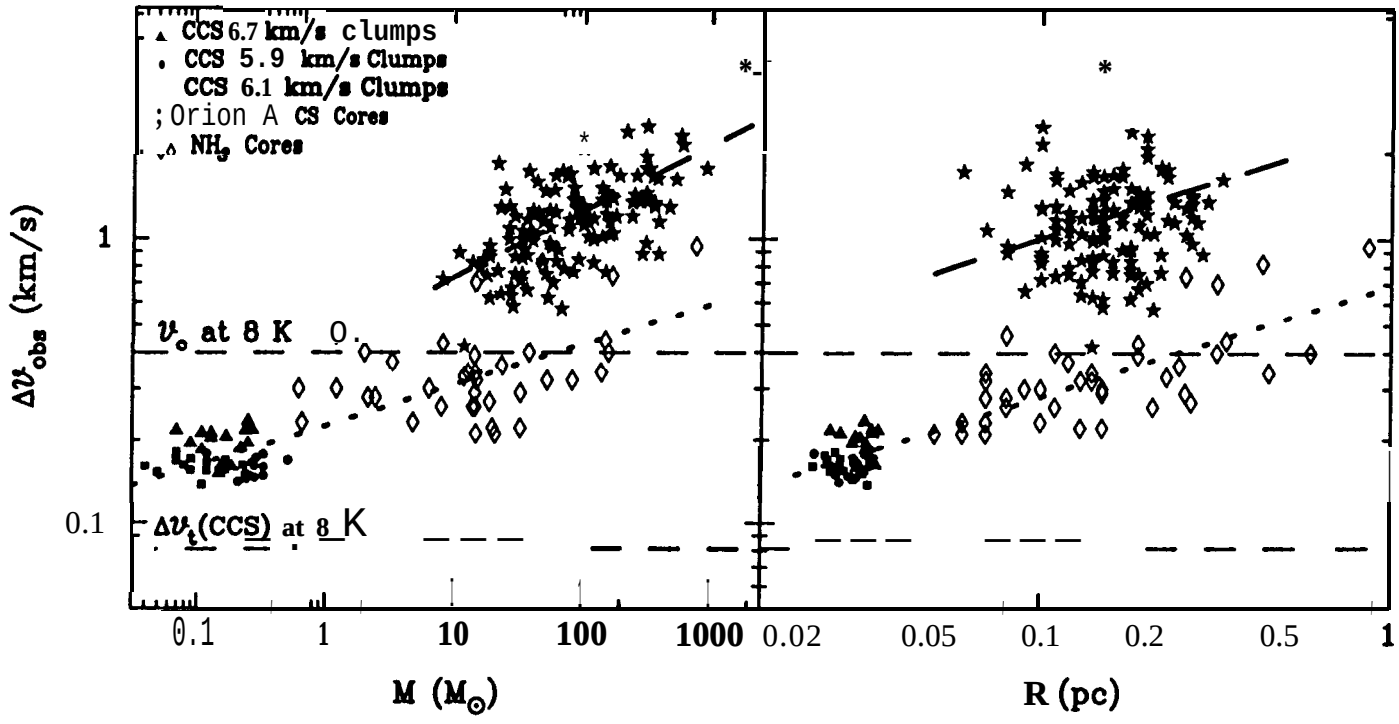
CCS 6.7 km/s clumps
CCS 5.9 km/s Clumps
CCS 6.1 km/s Clumps
Orion A CS Cores
NH3 Cores
1
0.1
Δv_obs (km/s)
v_o at 8 K
Δv_t(CCS) at 8 K
0.1
1
10
100
1000
M (M_⊙)
0.02
0.05
0.1
0.2
0.5
1
R (pc)

FIGURE 3

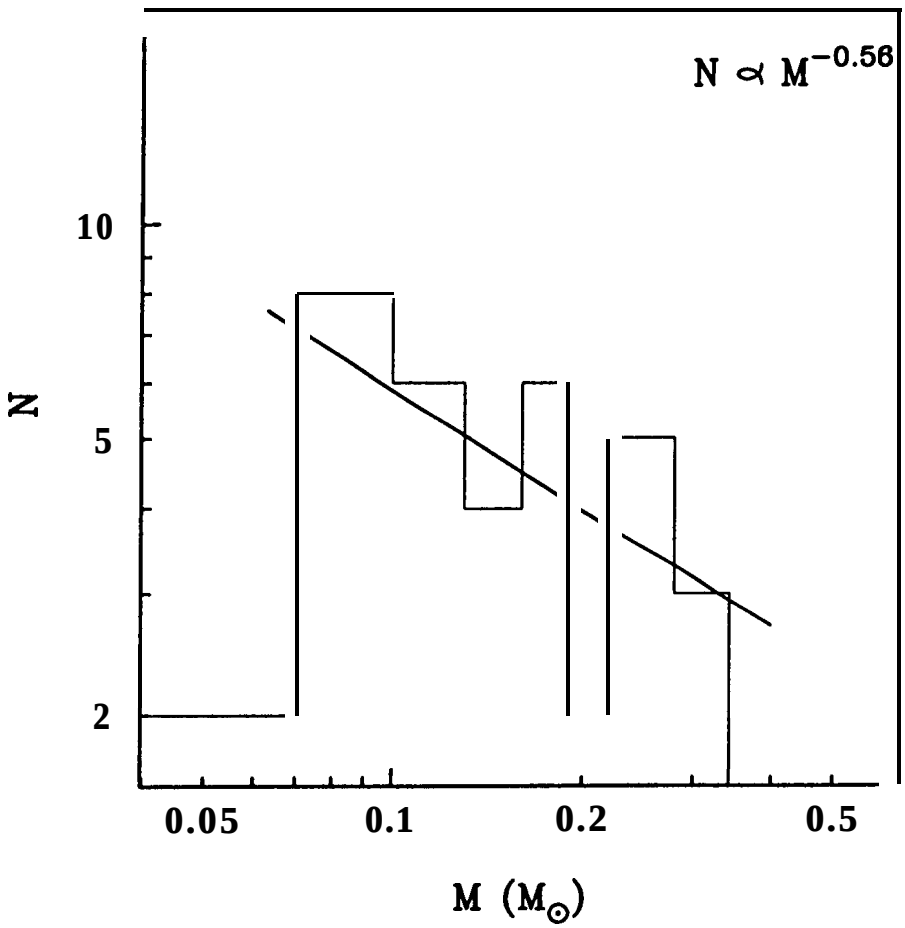

FIGURE 4